Characterisation of Zeolitic Materials with a HEU-Type Structure Modified by Transition Metal Elements: Definition of Acid Sites in Nickel-Loaded Crystals in the Light of Experimental and Quantum-Chemical Results

A. Godelitsas,[b] D. Charistos,[a] A. Tsipis,[a] C. Tsipis,*[a] A. Filippidis,[c] C. Triantafyllidis,[d] G. Manos,[e] and D. Siapkas[f]

Abstract: Nickel-loaded HEU-type zeolite crystals have been obtained by well-known synthetic procedures and characterised by X-ray fluorescence (XRF), scanning-electron microscopy/ energy-dispersive spectroscopy (SEM-EDS), FT-IR, diffuse reflectance UV/ Vis spectroscopy (DR(UV/Vis)S) and X-ray photoelectron spectroscopy (XPS) measurements as non-homoionic and non-stoichiometric substances containing exchangeable hydrated Ni^{2+} ions in the micropores and nickel hydroxide phases supported on the surface. Thermogravimetric analysis/ differential gravimetry (TGA/DTG) and differential thermal analysis (DTA) demonstrated that full dehydration below approximately $400\,°C$ follows a clearly endothermic process, whereas at higher temperatures the zeolite is amorphised and finally partially recrystallised to Ni(Al,Si) oxides, detected by powder X-ray powder diffraction (XRD). The solid acidity of NiHEU, initially determined by temperature-programmed desorption (TPD) of ammonia to be $8.93\ \mathrm{mg\,g^{-1}}\ NH_3$, is attributed to the weak acid sites (fundamentally Lewis sites) resolved at approximately $183\,°C$, and to the strong acid sites (essentially Brønsted sites) resolved at approximately $461\,°C$ in the TPD pattern. A more sophisticated study based on in situ/ex situ FT-IR with in situ/ex situ ^{27}Al MAS NMR and pyridine (Py) as a probe molecule, revealed that the Lewis acid sites can be attributed primarily to Ni^{2+} ions, whereas the Brønsted ones can probably be associated with the surface-supported nickel hydroxide phases. The spectroscopic measurements in conjunction with powder XRD and ^{29}Si MAS NMR data strongly suggest that distorted Al tetrahedra are formed during the dehydration process and Py chemisorption/complexation (NiHEU-Py), whereas the crystal structure is remarkably well preserved in the rehydrated material (NiHEU-Py/R). The structural, electronic, energetic and spectroscopic properties of all possible nickel(II) aqua and dihydroxy complexes absorbed in the zeolite micropores or supported on the zeolite surface were studied theoretically by density functional theory (DFT). The computed proton affinity, found to be in the range $182.0 – 210.0\ \mathrm{kcal\,mol^{-1}}$, increases with increasing coordination number of the aqua and dihydroxy nickel(II) complexes.

Introduction

HEU-type zeolites, a family of crystalline aluminosilicate microporous solids, include both natural and synthetic members.[1, 2] The naturally occurring HEU-type zeolites (heulandite – clinoptilolite series) are the most abundant minerals on Earth, exhibiting a zeolitic structure. They are mostly found in specific types of sedimentary rocks (tuffs) in

[a] Prof. Dr. C. Tsipis, Dr. D. Charistos, Dr. A. Tsipis
Department of General and Inorganic Chemistry, Faculty of Chemistry
Aristotle University of Thessaloniki, 54006 Thessaloniki (Greece)
Fax: (+31) 997851
E-mail: tsipis@chem.auth.gr

[b] Dr. A. Godelitsas
TVX Hellas S.A.
63082 Stratoni, Chalkidiki (Greece)

[c] Prof. Dr. A. Filippidis
Department of Mineralogy – Petrology – Economic Geology
Faculty of Geology
Aristotle University of Thessaloniki, 54006 Thessaloniki (Greece)

[d] Dr. C. Triantafyllidis
Department of Chemistry, University of Ioannina
45110 Ioannina (Greece)

[e] Dr. G. Manos
Department of Chemical Engineering, University College London
London WC1E 7JE (UK)

[f] Dr. D. Siapkas
Department of Solid State Physics, Faculty of Physics
Aristotle University of Thessaloniki, 54006 Thessaloniki (Greece)

Supporting information (DR(UV/Vis) and FTIR absorption spectra of NaHEU and NiHEU, and in situ FTIR absorption and ^{27}Al MAS NMR spectra of NiHEU-Py and NiHEU-Py. Tables list the computed excitation energies, oscillator strengths, harmonic vibrational frequencies and IR intensities for the high-spin ground states of $[Ni(OH_2)_n]^{2+}$ and $[Ni(OH_2)_{n-2}(OH)_2]$ ($n=4-6$) complexes) for this article is available on the WWW under http://www.wiley-vch.de/home/chemistry/ or from the author.

the form of small crystals (0.1–100 μm) associated with clays and other silicate and aluminosilicate phases of similar density.[3–6] However, even centimetre-scale single crystals can grow in cavities of igneous rocks (for example, basalts) from natural hydrothermal solutions. Tuffs containing crystals of HEU-type zeolites (zeoliferous rocks) form large deposits in many areas, such as the USA, Japan, the former Soviet Union, Hungary, Bulgaria, Australia, China, Greece and Mexico, and are low-cost industrial minerals with several commercial applications.[6–12] The synthetic zeolite species,[13–16] including LZ-219 and CIT-3, are all more expensive microporous solids, as yet without extensive practical applications.

The crystal structure[17] of all HEU-type zeolites (both natural and synthetic) is characterised by a three-dimensional aluminosilicate framework consisting fundamentally of secondary building units (SBUs) of the 4-4-1 type, formed by TO$_4$ (T = Si, Al) tetrahedral primary building units (PBUs)[2]. Chain-like structural subunits (SSUs) of the *he* type originate from these SBUs, and are further combined through *4.5²*-type SSUs to form structural "sheets" parallel to the (010) (*ac*) plane.[18–20] For this spatial arrangement of SSUs, the framework contains narrow four- and five-membered rings, as well as broad eight- and ten-membered rings constituting intra-framework micropores (channels) capable of hosting extra-framework/exchangeable cations (for example, Na⁺, K⁺, Ca²⁺) in association with mobile water molecules. The monoclinic (*C2/m*) crystals of HEU-type zeolites accommodate two different systems of micropores interconnected within the lattice, the first developed along the [001] *c* axis with both eight- and ten-membered rings forming A- and

B-type channels (3.3 × 4.6 and 3.0 × 7.6 Å respectively), and the second developed along the [102] *a* axis with eight-membered rings forming C-type channels (2.6 × 4.7 Å).

The relatively "open" structure of HEU-type zeolites, with a total pore volume (TPV) of 35%,[6] enhances the sorption properties of these microporous solids, especially towards gaseous molecules such as dinitrogen, water, carbon monoxide, ammonia, methanol, methane and pyridine, which are small enough to enter the channels. The TPV of zeolite crystals is correlated with the crystallographic arrangement of the aluminosilicate framework, and particularly with the framework density (FD), which is 17.0 T sites/1000 Å³ for the HEU-type structure.[2] However, the chemical composition of the framework (the Si/Al ratio, in the range 3–5) modulates the ion-exchange properties of the zeolites expressed as cation-exchange capacity (CEC, which can theoretically reach 330 meq/100 g).[21] The rather low Si/Al ratio and the consequently increased CEC render HEU-type zeolites advantageous for binding dissolved cations from aqueous solutions. Of particular interest is the interaction of HEU-type zeolites with metallic cations (mostly heavy metals) such as lead, cadmium, zinc, copper and nickel, which are sorbed by the zeolite and immobilised in the crystals, modifying the initial HEU-type structure. This is crucial for environmental technology (for example, decontamination of wastewaters) and for certain industrial applications. In the development of transition metal based catalysts, precise characterisation of the chemically modified (metal-loaded) zeolite and thorough investigation of the chemical properties of the solid, with particular emphasis on the definition of potential structural Lewis- and/or Brønsted-type active sites, are essential.

To our knowledge, nickel-loaded HEU-type zeolites, in contrast to their copper counterparts, have not been extensively studied, in spite of their importance in heterogeneous catalytic processes. The results reported until now[22] deal mainly with nickel-loaded HEU-type zeolites coexisting in zeoliferous rocks with different silicate and aluminosilicate minerals. These measurements must be treated with caution, since nickel interacts with crystals of all the associated phases (for example, clays) in the preparation process. Although the crystal structures of pure HEU-type zeolites ion-exchanged with several metals (Na, K, Rb, Cs, Mg, Sr, Ba, Mn, Ag, Cd, Tl, Pb) have been determined,[23] the crystal structure of the fully or even the partially nickel-exchanged form has not been reported. We have already published a few preliminary results concerning the structural and chemical properties of natural zeolite crystals modified with nickel,[24] and here we report further details of the characterisation of pure natural HEU-type zeolite crystals loaded with nickel by means of known wet-chemical procedures. We had four objectives: 1) characterisation of these crystals using an appropriate combination of microscopic (scanning-electron microscopy/energy-dispersive spectroscopy (SEM-EDS)), diffraction (powder X-ray diffraction (XRD)), thermal (temperature-programmed desorption (TPD), thermogravimetric analysis/differential gravimetry (TGA/DTG) and differential thermal analysis (DTA)) and spectroscopic (radioisotope-induced X-ray fluorescence (RI-XRF), diffuse reflectance spectroscopy (DRS), X-ray photoelectron spectroscopy (XPS), ²⁹Si MAS NMR, in situ/ex

Abstract in Greek:

Περίληψη: Κρύσταλλοι HEU-τύπου ζεόλιθου φορτωμένου με Ni ελήφθησαν με βάση κοινές μεθόδους σύνθεσης και χαρακτηρίσθηκαν, με μετρήσεις XRF, SEM-EDS, FT-IR, DR(UV-Vis) και XPS, ως μη-ομοϊοντικοί και μη-στοιχειομετρικοί, που περιέχουν ανταλλάξιμα εφυδατωμένα ιόντα Ni²⁺ μέσα στους μικροπόρους και φάσεις υδροξειδίου του νικελίου στην επιφάνεια. Μετρήσεις TGA/DTG και DTA έδειξαν ότι σε θερμοκρασία μικρότερη των 400 °C συμβαίνει πλήρης αφυδάτωση που συνοδεύεται από καθαρή ενδόθερμη διεργασία, ενώ σε υψηλότερες θερμοκρασίες ο ζεόλιθος καθίσταται άμορφος και τελικά ανακρυσταλλώνεται με τη μορφή οξειδίων Ni(Al,Si). Η στερεή οξύτητα του ζεόλιθου NiHEU, που υπολογίσθηκε αρχικά με TPD της αμμωνίας σε 8,93 mg g⁻¹ NH₃, αποδόθηκε τόσο σε ασθενείς όξινες θέσεις (στην ουσία θέσεις Lewis) που αναλύθηκαν σε θερμοκρασία 183 °C, όσο και σε ισχυρές όξινες θέσεις (στην ουσία θέσεις Brønsted) που αναλύθηκαν σε θερμοκρασία 461 °C στο πρότυπο TPD. Μια πιο εξειδικευμένη μελέτη βασισμένη σε συνδυασμό in-situ/ex-situ FT-IR και in-situ/ex-situ ²⁷Al MAS NMR με πυριδίνη (Py) ως μόριο αναφοράς, έδειξε ότι οι όξινες θέσεις Lewis μπορεί να αποδοθούν στα ιόντα Ni²⁺, ενώ οι θέσεις Brønsted θα μπορούσαν πιθανόν να αποδοθούν σε φάσεις υδροξειδίου του νικελίου που βρίσκονται στην επιφάνεια του ζεόλιθου. Οι φασματοσκοπικές μετρήσεις σε συνδυασμό με μετρήσεις XRD-σκόνης και ²⁹Si MAS NMR έδειξαν το σχηματισμό παραμορφωμένων αργιλικών τετραέδρων κατά την αφυδάτωση και χημειορρόφηση/συμπλοκοποίηση της πυριδίνης (NiHEU-Py), ενώ η κρυσταλλική δομή διατηρείται σε σημαντικό βαθμό στο αφυδατωμένο υλικό (NiHEU-Py/R). Οι δομικές, ηλεκτρονικές, ενεργειακές και φασματοσκοπικές ιδιότητες όλων των πιθανών υδατο- και υδατο-διυδροξυ-συμπλόκων του Ni²⁺, μελετήθηκαν θεωρητικά με βάση τη μέθοδο DFT. Οι πρωτονιοσυγγένειες που υπολογίσθηκαν βρίσκονται στην περιοχή των 182,0 μ 210,0 kcal mol⁻¹ και αυξάνονται με την αύξηση του αριθμού συναρμογής των υδατο- και υδατο-διυδροξυ-συμπλόκων του Ni²⁺.

 Chem. Eur. J. **2001**, *7*, No. 17

situ FT-IR, in situ/ex situ ^{27}Al MAS NMR spectroscopic) techniques; 2) definition of the acid sites created in the structure of the microporous solid by nickel; 3) exploration, by first-principle quantum-chemical methods, of the structural, electronic and spectroscopic properties of the nickel-containing species sorbed or surface-precipitated on the zeolite structure; 4) investigation of the efficiency of HEU-type zeolites in the removal of dissolved nickel ions from aqueous media, which is of considerable technological and environmental significance.

Experimental Section

Starting material: The HEU-type zeolite sample was of natural origin, occurring in geodes of a basaltic rock. Pure, pale white, single crystals were detached carefully from the rock, cleaned in an ultrasonic bath with distilled water, air-dried and crushed in an agate mortar. A granular fraction, particle size 20 – 90 μm, which was selected taking into account the average size of HEU-type zeolite crystals in relevant commercial products (zeoliferous rocks), was separated with standard analytical sieves.

Preparation of nickel-loaded (NiHEU) material: The preparation of this material was based on known procedures[23h, 23l] for heavy metal-loaded/ion-exchanged HEU-type zeolites, through appropriate modification of the homoionic sodium form (fully Na$^+$-exchanged), which is a precursor phase (NaHEU). In particular, the previously prepared NaHEU crystals were refluxed repeatedly with a concentrated aqueous solution[22h] of Ni(NO$_3$)$_2$ to achieve the maximum release of Na$^+$ ions (checked in the filtrates by flame photometry; Bruno Lange M6a), the only exchangeable cation in the NaHEU. The NiHEU crystals (pale green) were collected by filtration, washed with small portions of distilled water until no traces of nickel were detected in the filtrates by atomic absorption spectrometry (Perkin-Elmer 5000), and stored in a desiccator over a saturated solution of Ca(NO$_3$)$_2$.

Spectroscopic and thermogravimetric characterisation: Preliminary characterisation of NiHEU was by powder XRD (Scintag XDS2000, Cu$_{Ka}$, $2\theta = 2° – 80°$, $1°$ min^{-1}) and SEM-EDS (JEOL JSM 840-A equipped with an Oxford ISIS 300 EDS) also using carbon-coated polished sections of the crystals. The total nickel content of the solid was determined directly by RI-XRF using an ^{241}Am secondary excitation source (Sn target) and a Canberra LEGe detector with a 2-mil (2×10^{-3} inch) Be window connected to a computer-based data acquisition/MCA system (Canberra S-100). The initial spectroscopic study of the chemically modified zeolite was performed by FT-IR (Bruker IFS113v, KBr pellets) and DR(UV/Vis) (Shimadzu UV/Vis 2101 scanning spectrometer, BaSO$_4$ reference material). The surface of the material (up to approximately 30 Å) was investigated by XPS (V.G. Scientific 1000 instrument, Mg$_{Ka}$ X-ray source, 10^{-9} Torr UHV chamber), whereas characterisation of the aluminosilicate framework of the crystal structure was based on ^{29}Si and ^{27}Al MAS NMR on Bruker MSL 400 equipment with (CH$_3$)$_4$Si and [Al(H$_2$O)$_6$]$^{3+}$ reference materials. TGA/DTG and DTA were carried out with a Chan instrument in a He atmosphere at 20 °C min^{-1} up to 800 °C. The NiHEU samples obtained by the thermal analyses were also investigated by SEM-EDS and powder XRD.

Solid acidity of the NiHEU zeolite: This was determined by TPD of ammonia using a high-temperature vertical furnace with a temperature controller and a quartz vertical reactor equipped with a thermal conductivity detector (TCD) to determine the ammonia evolved. The material (100 mg) was placed in the reactor and dehydrated at 350 °C under a continuous flow of He (50 mL min^{-1}) for 3 h. The temperature was then lowered to 100 °C and dry ammonia was passed through the sample at 1.5 bar for 1 h. Physisorbed ammonia was also stripped at 100 °C under the He flow for 30 min. Chemisorbed ammonia was desorbed by heating the sample from 100 to 800 °C (heating rate 10 °C min^{-1}, He flow 50 mL min^{-1}) and a known amount of HCl solution was used for titrimetric determination after passage through the detector. The acid sites responsible for the solid acidity of the dehydrated (activated) NiHEU crystals were defined by in situ FT-IR and ^{27}Al MAS NMR, with Py as a probe molecule.

For in situ FT-IR experiments, thin self-supporting NiHEU wafers (approximately 14 mg cm^{-2}) were prepared and mounted within a special vacuum cell containing an internal electrically heated furnace region and appropriate windows for FT-IR measurements, adapted for a Mattson Cygnus 100 FT-IR spectrometer. The NiHEU samples were dehydrated at 350 °C under vacuum (10^{-5} Torr) for 12 h. The temperature was decreased to 150 °C to record the spectra of the activated zeolite. By continuous adjustment to ensure this temperature, a portion of spectroscopic-grade pyridine (3 μL), purified by several "freeze – pump – thaw" cycles to remove dissolved gases, was inserted by syringe in the vacuum cell and the in situ FT-IR spectra of NiHEU-Py were recorded. At that temperature pyridine is gaseous and can be chemisorbed by the zeolite. However, to remove possible physisorbed pyridine the pressure (initially 10^{-5} Torr) was decreased rapidly before the spectra were recorded, then the wafers were removed from the vacuum cell and the material was rehydrated for two weeks in the desiccator. The rehydrated sample (NiHEU-Py/R) was investigated by ex situ FT-IR (with KBr pellets), SEM-EDS, powder XRD, ^{29}Si MAS NMR and ^{27}Al MAS NMR.

Analogous experiments were performed using in situ ^{27}Al MAS NMR. NiHEU (an appropriate quantity) was inserted in a specially designed aluminium-free Pyrex glass tube, which was joined to a Schlenk-type vacuum line. The sample was dehydrated in a convenient vertical ceramic furnace at 350 °C for 12 h and then cooled to 150 °C for sorption of pyridine. After the reaction was complete the upper part of the tube, connected to the vacuum line, was first sealed using a flame. The lower part of the separated tube containing the NiHEU-Py material was sealed later with a sharp flame while being rotated continuously in liquid nitrogen to prevent the high temperature from affecting the sample and to obtain a well-shaped glass capsule. This capsule was mounted in a MAS zirconia rotor fitted on the Bruker MSL 400 spectrometer. After acquisition of the spectra, the capsule was crushed carefully and its contents were rehydrated (NiHEU-Py/R) for two weeks in the constant-humidity chamber for further examination by ex situ ^{27}Al MAS NMR, SEM-EDS, powder XRD, FT-IR and ^{29}Si MAS NMR.

Computational Details

The structural, electronic and energetic properties of all possible nickel(II) aqua and dihydroxy complexes absorbed in the zeolite micropores or supported on the zeolite surface, in both their low- (singlet) and high-spin (triplet) states, were computed using density functional theory (DFT) at the B3LYP level of theory (B3LYP = Becke's three-parameter hybrid functional[25] combined with the Lee – Yang – Parr correlation functional), using the LANL2DZ basis set that includes Dunning/Huzinaga full double zeta (DZ) basis on the first row and Los Alamos effective core potentials (ECPs) plus DZ for the nickel atom. The hybrid B3LYP functional gives acceptable results for molecular energies and geometries, as well as proton donation, and weak and strong hydrogen bonds.[26] No constraints were imposed on the geometry in any of the computations. Full geometry optimisation was performed for each structure using Schlegel's analytical gradient method,[27] and the attainment of the energy minimum was verified by calculating the vibrational frequencies that resulted in the absence of imaginary eigenvalues of the Hessian matrix. The vibrational modes and the corresponding frequencies were based on a harmonic force field. Electronic transitions were computed by the configuration interaction (CI) singles approach. All calculations were performed with the Gaussian 98 program suite.[28]

Results and Discussion

Characterisation of zeolitic materials with a HEU-type structure modified by Ni^{2+} ions: The total nickel content of the nickel-loaded HEU-type zeolite, determined by RI-XRF, was 3.5 % (w/w) (35 mg g^{-1}). The calculated CEC of the precursor NaHEU zeolite (302 meq/100 g) strongly suggests that the completely nickel-exchanged NiHEU material could

theoretically contain 88.62 mg g^{-1} nickel. However, if one assumes that Ni^{2+} ions had been sorbed through ion exchange, the product would primarily be a partially nickel-exchanged (non-homoionic) zeolitic material. Bulk analyses of the material showed that a considerable amount of sodium remained in the crystal structure of NiHEU. SEM-EDS of polished sections of the material indicated that the distribution of nickel was remarkably inhomogeneous throughout the grains, with significant accumulation towards the rims and around the edges (Figure 1). This means that the non-homoionic NiHEU crystals were also non-stoichiometric, so
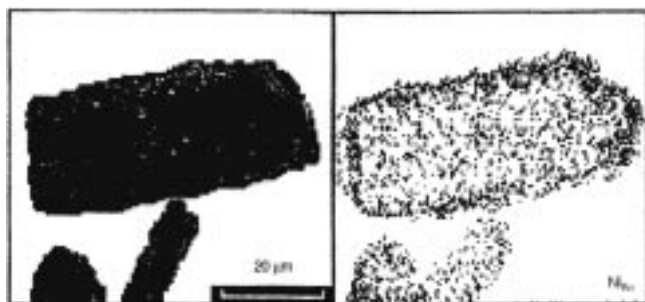
Figure 1. SEM-EDS results, indicating the distribution of nickel in polished sections of NiHEU crystals (Ni$_{K\alpha}$· was used for the corresponding elemental mapping). Left: typical SEM image (back-scattered electron images) of NiHEU crystal sections. Right: typical elemental mapping of the nickel distribution.

the nickel sorption by the zeolite may not be completely attributable to ion exchange. The XPS study (Figure 2) showed that the near-surface layers of the material comprised not Ni^{2+} ions but specific compounds corresponding to hydroxides of nickel(II)[29–32] (Ni 2p$_{3/2}$ peak resolved at
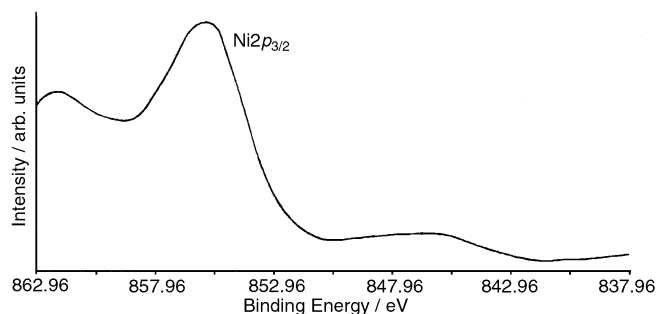

Figure 2. Ni 2p$_{3/2}$ region of the XPS spectrum of NiHEU.

856 eV). This is further supported by observation of an extra characteristic sharp band at 1384 cm^{-1} in the FT-IR spectra of NiHEU, associated[33] with the δ(OH) stretching vibrations of metal hydroxides and/or oxyhydroxides. These data are further verified by SEM-EDS investigation of individual NiHEU crystals, indicating the presence of very small (up to 2 µm) solid nickel phases supported on the zeolite surface (Figure 3). In addition, the powder XRD study of NiHEU, NaHEU and pure nickel hydroxide proved the crystalline nature of the surface nickel hydroxide phases, by definition of small, well-resolved peaks in the corresponding patterns
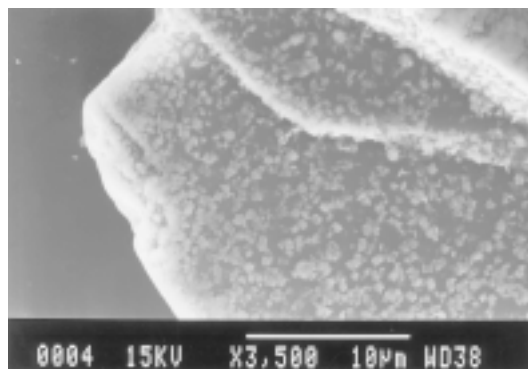

Figure 3. SEM image showing the nickel hydroxide phases supported on the surface of NiHEU.

which were not due to the structure of the HEU-type zeolitic substrate.[34]

The NiHEU zeolitic material is not a typical partially nickel-exchanged (non-homoionic) form of a HEU-type zeolite, and the non-stoichiometric nickel-loaded crystals have possibly been formed through metal sorption mechanisms, which do not exclusively involve ion exchange. These mechanisms are mainly represented by distinct surface chemical processes, such as adsorption and surface precipitation,[35, 36] taking place at the solid–solution interface during treatment of the zeolite with aqueous solutions of Ni^{2+} ions. These processes are facilitated by the hydrolysis of the Ni^{2+} ion,[37] which is favoured at the elevated temperature required for sufficient metal loading. As a result, various hydrolysis products interact progressively with the microporous solid, which can also act as a forceful cation exchanger. The positively charged solvated species, such as [Ni(H$_2$O)$_n$]$^{2+}$ and [NiOH]$^+$, are sorbed primarily through ion exchange. replacing initial extra-framework Na$^+$ ions, whereas mononuclear and/or polynuclear insoluble hydroxide species can be bonded to the material by surface precipitation. As a consequence, the NiHEU zeolite exhibits a rather complicated structure in which nickel ions occupying different sites in the micropores (channels) and on the surface possess differing Lewis and/or Brønsted acidic properties. Schoonheydt et al.[38] discussed adequately the crucial importance of such structures in possible catalytic applications with respect to non-stoichiometric nickel-loaded Linde NaX and NaY (NiFAU) synthetic zeolites. Accordingly, XPS measurements by Xiao and Meng[39] demonstrated that in nickel-containing HZSM-5 catalysts (NiMFI) nickel ions can exist in various other coordination environments as well as in nickel hydroxides supported on the surface. It is rather difficult to prepare either fully or even partially nickel-exchanged HEU-type zeolite crystals that are practically stoichiometric (with the same metal content in each unit cell) in order for the crystal structure to be resolved accurately and the positions of the ions in the lattice to be defined precisely.

As dipositive metal cations with small ionic radii are preferentially surrounded by H$_2$O molecules and are less coordinated by framework O atoms, in the nickel-loaded HEU-type zeolite Ni^{2+} ions with an ionic radius of 0.70 Å[40] are expected to be completely surrounded by water molecules

in the large micropores (A and B), probably without coordination by framework O atoms. The existence of hydrated Ni^{2+} ions in the structure of NiHEU is further supported by the DR(UV/Vis) spectra showing a characteristic broad band in the 630–765 nm region and a band at 390 nm.[41] However, the ^{29}Si and ^{27}Al MAS NMR spectra of NiHEU (Figures 4 and 5) are identical to those of the raw HEU-type zeolite,[42–44] strongly suggesting that the aluminosilicate framework hosting the extra-framework hydrated Ni^{2+} ions has not been affected by the sorption of nickel ions. The Si/Al ratio of NiHEU calculated from ^{29}Si and ^{27}Al MAS NMR spectra[42] is 3.78.
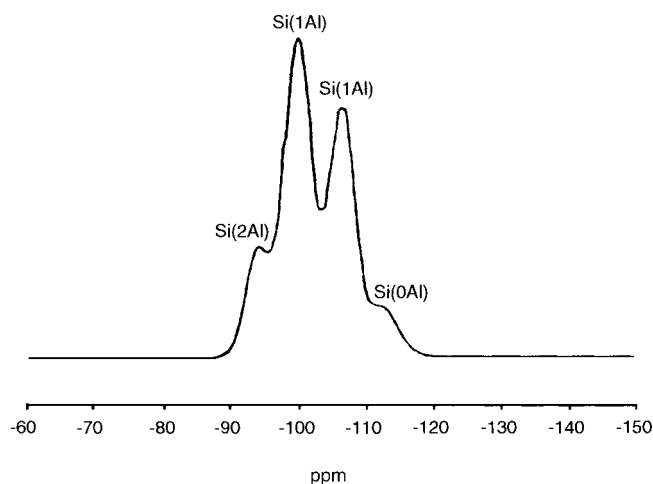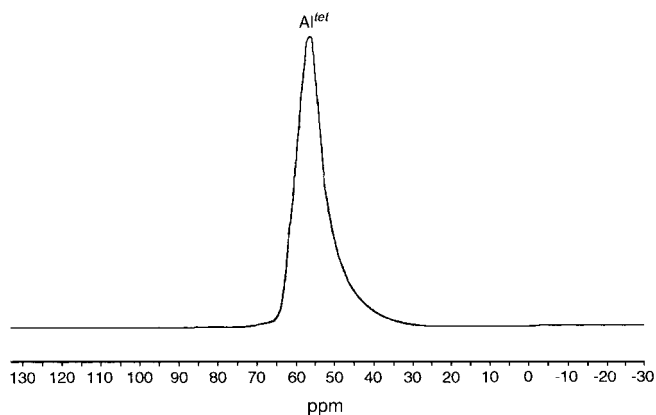

Figure 4. ^{29}Si MAS NMR spectrum of NiHEU.

Figure 5. ^{27}Al MAS NMR spectrum of NiHEU.

Definition of acid sites in nickel-loaded HEU-type zeolite: The Ni^{2+} ions encapsulated in the structure of NiHEU introduce a weak solid acidity to the material that can easily be recognised after suitable thermal treatment (activation), which leads to the removal of the coordinated water molecules and the creation of Lewis acid sites due to the dehydrated Ni^{2+} ions.[45–48] However, the nickel hydroxide phases supported on the surface of the crystals seem to play a more critical role in the solid acidity, for they tend to constitute Brønsted acid sites, adding stronger acidity to the nickel-loaded zeolite. The thermal analyses of NiHEU (Figure 6) revealed a total weight loss of 15.93% involving
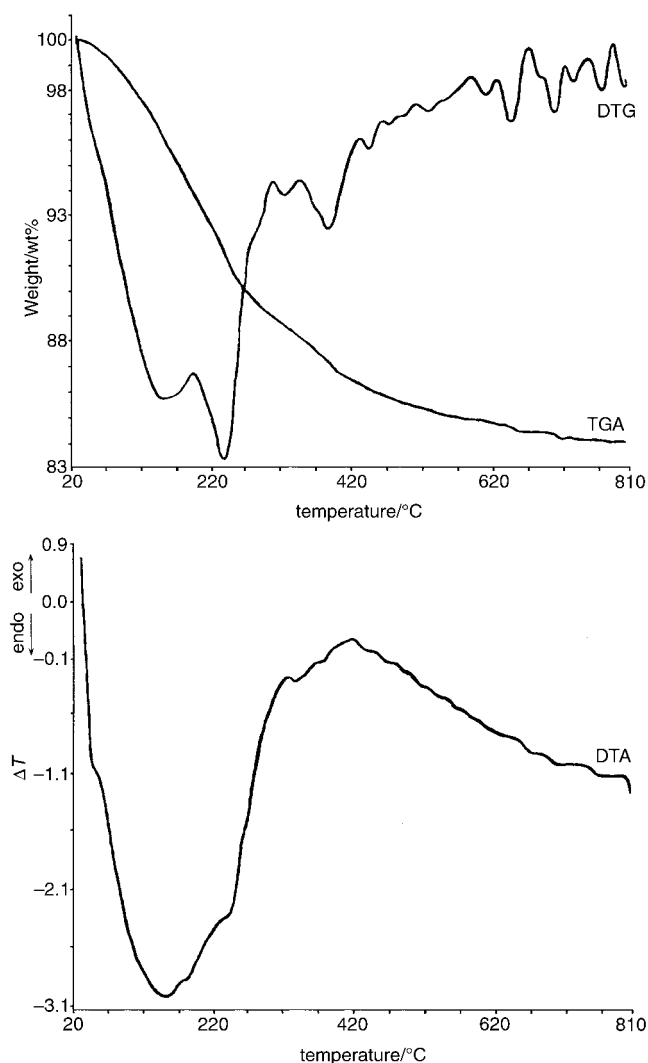

Figure 6. TGA/DTG (top) and DTA (bottom) curves of NiHEU.

three main stages, but complete dehydration of the crystals was realised below approximately 400 °C corresponding to a major weight loss of approximately1 3%. A discrete endothermic event resolved in the DTA curve at 150 °C is evidently related to the release of zeolitic H_2O molecules predominantly associated with the Ni^{2+} ions in the micropores (Figure 6 bottom). The minor weight loss (2.93%) from approximately 400 to 800 °C could be attributed to dehydroxylation of the surface-supported nickel hydroxide phases, which was a potential source of volatile constituents that could be released at higher temperatures. The SEM-EDS examination of the thermally treated NiHEU showed that the grains obtained retained the external morphology of the initial zeolite crystals, but the powder XRD data indicated that the solid had become practically amorphous. However, careful treatment of the powder XRD patterns revealed the presence of a small sharp peak, separated from the background, which corresponded to crystalline Ni(Al,Si) oxides. Partial recrystallisation evidently takes place as a result of the progressive reaction of the dehydroxylated nickel hydroxide phases with the amorphised zeolitic substrate. These results imply that complete dehydration (activation) of NiHEU,

which is required for identifying the acid sites by TPD and in situ FT-IR/MAS NMR spectroscopy, can be achieved reasonably well at quite low temperatures (below approximately 400 °C). TPD of ammonia gave a considerable total solid acidity of NiHEU (8.93 mg NH$_3$ g^{-1}). The characterisation of zeolitic materials with a modified structure using TPD could also provide valuable information on the strength distribution of the acid sites recorded.[45–48] Thus the broad peak in the TPD pattern (Figure 7) with a maximum at 183 °C corresponds to "weak" acid sites, which are represented mainly by
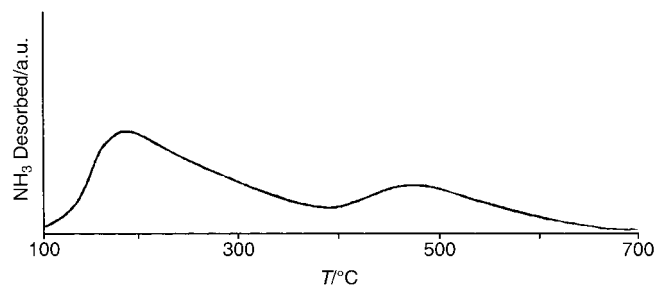

Figure 7. TPD of NH$_3$ from NiHEU activated at 350 °C.

Lewis-type sites such as the dehydrated Ni^{2+} ions. Associated acid sites are also considered to be any relevant extra-framework species located in the micropores (that is, the residual Na$^+$ ions), including potential Al^{3+} ions in an octahedral coordination environment (Al^{oct}), which can be formed in activated zeolites. The second broad peak in the TPD spectrum, with a maximum at 461 °C, corresponds to "strong" acid sites, which are primarily attributed to Brønsted-type sites containing protonated active groups. The characteristic Brønsted-type sites in the structure of activated zeolites are the so-called bridging hydroxy groups, consisting of protons bonded to the aluminosilicate framework in the micropores (Si-O(H)-Al). However, possible silanol groups (Si−OH) commonly formed on the surface of zeolites (terminal hydroxy groups) do not constitute "strong" acid sites and are generally of minor importance. Extended bridging hydroxy groups are usually created in NH$_4^+$-exchanged zeolites as a result of the release of NH$_3$(g) during the thermal treatment, but are not typical of metal-loaded zeolites. Therefore, in NiHEU the "strong" acid sites observed in the TPD pattern are probably due to the surface-supported nickel hydroxides.

The different types of acid sites were characterised further by in situ FT-IR after exposure of the activated metal-loaded zeolite to gaseous strong electron donor ligands such as pyridine (Py).[49] The FTIR showed clearly that Py is chemisorbed on the activated NiHEU zeolite through reaction with certain structural acid sites of the zeolite. The lack of discrete absorption bands in the 3700–3500 cm^{-1} region indicates the absence of Brønsted-type acid sites attributable to bridging hydroxy groups. In contrast, some absorption bands appearing in the 1700–1400 cm^{-1} region strongly suggest that Py can also be chemisorbed to Lewis and/or Brønsted acid sites different from those of the bridging hydroxy groups. The normal vibrational modes with maxima at 1610 cm^{-1} and 1447 cm^{-1} are due to the species resulting

from the interaction of the lone-pair orbital of Py with the appropriate vacant orbital of the Lewis acid sites, whereas that at 1650 cm^{-1} is characteristic of the pyridinium ion formed by interaction of Py with the protons of the Brønsted acid sites. The band at 1491 cm^{-1} could be attributed to the pyridine ring and is common to all Py-containing species. These data substantiate the existence of "strong" Brønsted-type acid sites due to surface-supported nickel hydroxides, identified with certainty by a characteristic peak at 461 °C in the TPD spectrum of NiHEU (Figure 7). However, the Lewis-type acid sites, verified by FT-IR spectra of the NiHEU-Py material, could be due primarily to dehydrated Ni^{2+} ions located in the micropores, as well as to residual Na$^+$ ions. In addition, sufficient evidence for relevant acid sites due to extra-framework octahedrally coordinated Al^{3+} ions was obtained from ^{27}Al MAS NMR spectra. The in situ ^{27}Al MAS NMR spectrum of NiHEU-Py exhibits, besides the characteristic peak due to tetrahedral Al (Al^{tet}) moieties, a second broad peak at $\delta = 56$ also due to the presence of Al^{oct} moieties. Moreover, the ex situ ^{27}Al MAS NMR spectra recorded after rehydration of the material (forming NiHEU-Py/R) exhibited only the single peak due to Al^{tet}; hence no Al^{oct} moieties were created or remained in the rehydrated crystal structure. Consequently, distorted Al^{tet} primary building units (Al tetrahedra) are most probably formed in the aluminosilicate framework of the zeolite upon activation, then further rearranged. Therefore, the Lewis-type acid sites resolved in the in situ FT-IR spectra are represented solely by exchangeable cationic species and particularly by the dominant Ni^{2+} ions. A reversible structural transformation of this kind has not been reported previously for zeolites, but it is well known for other microporous materials, such as the zeotype AlPO$_4$.[50]

Chemisorption of the Lewis-type base Py on the activated NiHEU is apparently associated with coordination processes affording relevant Ni^{2+} coordination compounds throughout the crystals of the material (intra-zeolite and surface complexes). The powder XRD patterns of NiHEU-Py/R (Figure 8) demonstrated that the crystal structure of the zeolite is essentially preserved during dehydration/activation followed by Py sorption and rehydration. This is important for potential catalytic applications of HEU-type zeolites modified by Ni^{2+}
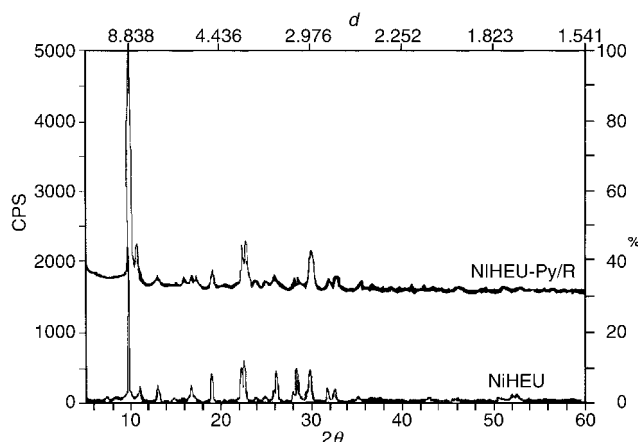

Figure 8. Powder XRD patterns of NiHEU-Py/R (top) and NiHEU (bottom).

ions,[22i] and it is also proved by the ex situ ^{29}Si MAS NMR and FT-IR spectra, which are identical to those of the starting NiHEU material.

Structural, energetic and electronic properties of [Ni(OH$_2$)$_n$]$^{2+}$ ($n = 4 – 6$) complexes: The Ni^{2+} ions may exist in their complexes both in high-spin (triplet) and low-spin (singlet) states. The ordering of spin states depends on the strength and symmetry of the ligand field. Figure 9, 10 and 11 present the optimised geometries for [Ni(OH$_2$)$_n$]$^{2+}$ ($n = 4 – 6$) complexes in both their singlet and triplet states.

[Ni(OH$_2$)$_4$]$^{2+}$ complexes: The low-spin state of the tetraaqua Ni^{II} cluster, [Ni(OH$_2$)$_4$]$^{2+}$(S), possessing D_{2h} symmetry, is a local minimum in the potential energy surface (PES) at 16.9 kcal mol^{-1} higher in energy than the high-spin ground state [Ni(OH$_2$)$_4$]$^{2+}$(T) (Figure 9). The H atoms of two coordinated water molecules in *trans* positions are in the square-planar coordination plane, whereas those of the other two coordinated water molecules are perpendicular to the plane. Moreover, the H atoms of the coordinated water molecules in *trans* positions adopt a staggered conformation, with dihedral angles for the two pairs of *trans* water ligands of 41.3° and 53.3°. All O-Ni-O bond angles are 90°. The H-O-H

bond angle of the coordinated water molecules is higher by about 8° than the corresponding angle of the free water molecule. The computed dipole moment (0.00 D) is consistent with the D_{2h} symmetry of the complex.

According to Mulliken population analysis the net atomic charges on the central Ni^{2+} ion, the O donor atoms and the H atoms are $+0.92$, -0.72 and $+0.50$ charge units, respectively. The bond overlap populations of the Ni$-$O and O$-$H bonds are 0.13 and 0.27 respectively. The HOMO at -0.661 eV corresponds to a central Ni^{2+} atom non-bonding MO, with predominantly d$_{z^2}$ character (Figure 12), whereas the LUMO at -0.496 eV corresponds to a central Ni^{2+} atom antibonding MO with predominantly d$_{x^2-y^2}$ character. Thus the HOMO–LUMO energy gap is only 0.165 eV, implying that a triplet state could also be possible as the ground state of the complex.

Indeed, we have found that the triplet state of the tetraaqua Ni^{II} cluster [Ni(OH$_2$)$_4$]$^{2+}$(T), corresponding to the global minimum in the PES, is the ground state of the complex. Application of crystal field theory leads one to expect that the energy of the d$_{x^2-y^2}$ orbital in a square-planar crystal field rises substantially as a consequence of strong repulsions between electrons of the metal and the ligands, and the low-spin state is expected to be the ground state. However, the B3LYP calculations demonstrated that the triplet state, adopting a distorted tetrahedral geometry (C_1 point group), becomes the ground state. The distorted tetrahedral geometry of the high-spin state is characterised by the dihedral angles: O(8)-Ni(1)-O(2)-O(3) 110.7, O(8)-Ni(1)-O(3)-O(11) 146.8, O(2)-Ni(1)-O(11)-O(3) 105.1°. Moreover, bond angles are O(2)-Ni(1)-O(3) 101.7° and O(8)-Ni(1)-O(11) 138.2° and the computed dipole moment is 0.55 D. The Ni$-$O bonds in the triplet state are about 0.1 Å longer than those of the square-planar singlet state. This is not unexpected, however, because the LUMO (d$_{x^2-y^2}$ of the central Ni^{2+} atom) involved in the bonding is a singly occupied molecular orbital (SOMO) in the triplet state, in which the Ni^{2+} ion and the O donor atoms acquire higher net atomic charges than in the singlet state (computed values $+1.16$ and -0.77 respectively). The positive net atomic charge on the H atoms remains unchanged. The bond overlap populations of the Ni$-$O bonds in the triplet state are 0.02 lower than those in the singlet state. The lower bond overlap population indicates
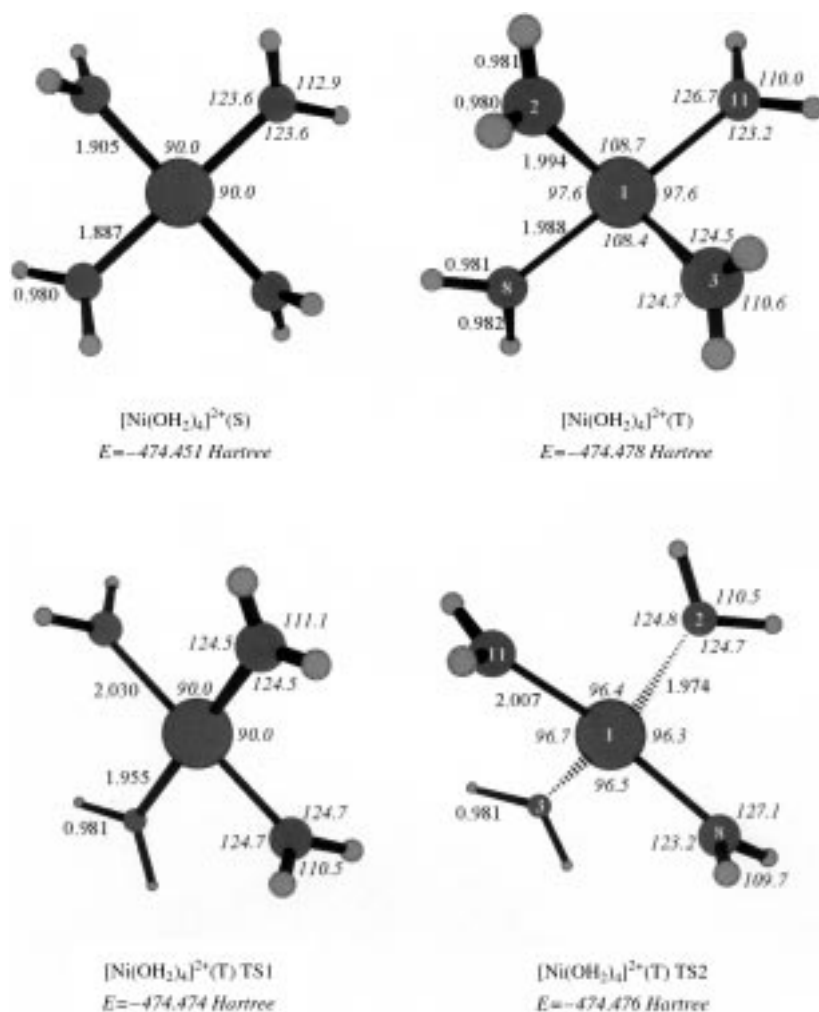

Figure 9. Optimised geometries of the [Ni(OH$_2$)$_4$]$^{2+}$ complexes in their low- and high-spin states computed at the B3LYP level of theory. Bond lengths in Å, bond angles (in italics) in °.

$[Ni(OH_2)_5]^{2+}(S)$

$E = -550.904$ Hartree

$[Ni(OH_2)_5]^{2+}(T)$, TS
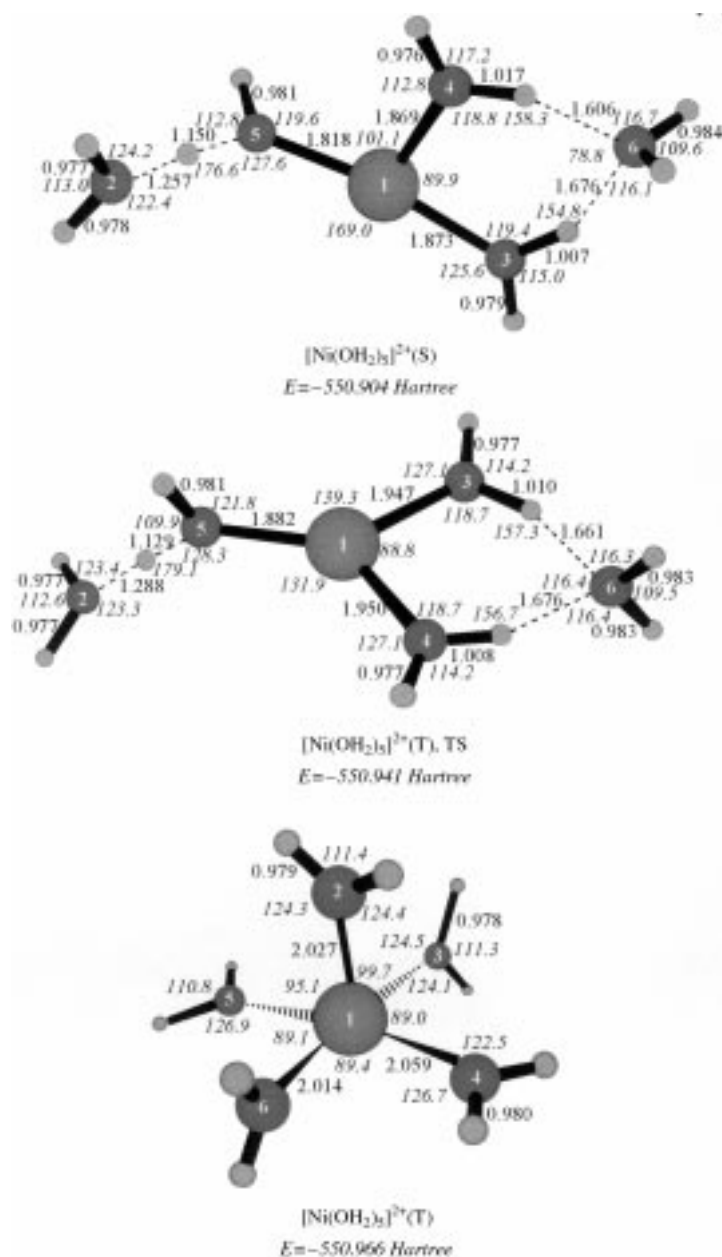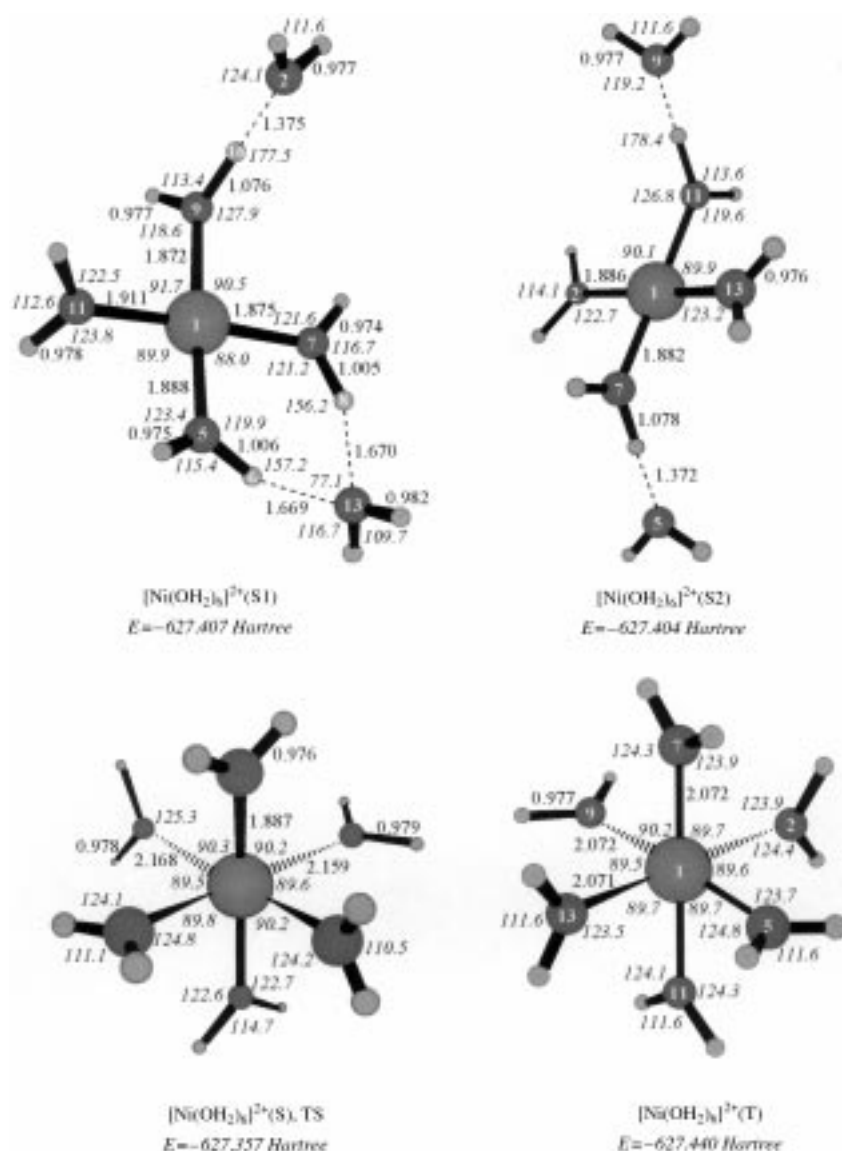
$E = -550.941$ Hartree

$[Ni(OH_2)_5]^{2+}(T)$

$E = -550.966$ Hartree

Figure 10. Optimised geometries of the $[Ni(OH_2)_5]^{2+}$ complexes in their low- and high-spin states computed at the B3LYP level of theory. Bond lengths in Å, bond angles (in italics) in °.

that Ni−O bonds in the triplet state are weaker, which is also reflected in the longer computed bond lengths. The total atomic spin density is located mainly on the central Ni^{2+} ion (1.81) and much less on the O donor atoms (0.04 – 0.05) (Figure 13). However, the computed isotropic Fermi contact couplings (IFCC values) are −17.6 to −35.6 MHz. The two doubly degenerate SOMOs at −0.698 eV correspond to antibonding MOs with predominantly d_{yz} and d_{xz} character, but the LUMO at −0.367 eV corresponds to a central Ni^{2+} atom antibonding MO with predominantly 4s character.

A distorted tetrahedral transition state (TS2) about 1.5 kcal mol^{-1} higher in energy was located on the PES, with two Ni−O bonds that are shorter, and two that are longer, than the corresponding bonds of the ground state. The TS2

structure is characterised by the dihedral angles: O(2)-Ni(1)-O(8)-O(3) 102.1, O(8)-Ni(1)-O(3)-O(11) 155.6, O(2)-Ni(1)-O(11)-O(3) 102.4°. The computed dipole moment is 0.47 D. Very close to TS2 (about 0.8 kcal mol^{-1} higher in energy), another transition state, TS1 (Figure 9), exhibiting a square-planar configuration (zero dipole moment), was located on the PES. In the square-planar triplet TS1 two of the *trans* Ni−O bonds are about 0.075 Å shorter than the other two. The salient feature of the structure of TS1 is the eclipsed conformation of the H atoms of the coordinated water molecules in *trans* positions. Even the triplet square-planar transition state is more stable than the singlet square-planar configuration of $[Ni(OH_2)_4]^{2+}$, which according to crystal field theory is predicted to be the ground state. It is clear that the excitation of an electron to the σ antibonding $d_{x^2-y^2}$ orbital introduces an imbalance to the square-planar configuration througha D_{2d} distortion, leading ultimately to a tetrahedral excited state (TS2), which then relaxes to the triplet ground state. The high-spin states of some Ni^{2+} and other transition metal ion complexes interacting with amino acid chains in various coordination geometries were recently predicted[51] to be the ground states at the DFT/B3LYP level of theory.

$[Ni(OH_2)_5]^{2+}$ complexes: The low-spin state of the pentaaqua Ni^{II} cluster, $[Ni(OH_2)_5]^{2+}(S)$, exhibiting a trigonal-planar geometry, is a local minimum in the PES at 38.9 kcal mol^{-1} higher in energy than the high-spin ground state $[Ni(OH_2)_5]^{2+}(T)$ (Figure 10). Surprisingly, two of the water molecules are not coordinated to the central Ni^{2+} ion, but are involved in the formation of short, strong hydrogen bonds with coordinated water molecules. Thus, the low-spin penta-aqua Ni^{II} cluster can be considered as a coordinatively unsaturated three-coordinate complex, $[Ni(OH_2)_3]^{2+} \cdot 2 H_2O$. The high-spin triplet state with an analogous trigonal planar geometry possesses one imaginary frequency and is therefore a transition state, $[Ni(OH_2)_5]^{2+}(T)$, TS (Figure 10). The salient feature of the trigonal-planar structures is the lengthening in the high-spin state by 0.06 – 0.08 Å of all Ni−O bonds. The geometry of the coordinated water ligands in both states remains unchanged.

In both electronic configurations one water molecule forms one short, strong hydrogen bond with a coordinated water molecule; the O−H, H···O bond lengths are 1.150, 1.257 Å and 1.129, 1.288 Å, and the O−H···O bond angle is 3.4° and 0.9°, in the low- and high-spin states, respectively. Another water molecule forms two weaker hydrogen bonds with the other two coordinated water molecules, one corresponding to O−H, H···O bond lengths of 1.017, 1.606 Å and 1.010, 1.661 Å and O−H···O bond angles of 21.7° and 22.7°, and the other to O−H, H···O bond lengths of 1.007, 1.678 Å and 1.008, 1.676 Å and O−H···O bond angles of 25.2° and 23.3°, for the low- and high-spin states, respectively. In the second case a six-membered chelate ring is formed.

In both pentaaqua Ni^{II} cluster structures, the Mulliken net atomic charges on the H atoms involved in hydrogen bond formation between the coordinated and non-coordinated water molecules are +0.53 and +0.50 charge units for the O−H···O and O−H···O···H−O skeletons, respectively. All other H atoms acquire a net atomic charge of +0.48 charge

$[Ni(OH_2)_6]^{2+}(S1)$
$E = -627.407\ Hartree$

$[Ni(OH_2)_6]^{2+}(S2)$
$E = -627.404\ Hartree$

Figure 13. Atomic spin density (0.002 a.u. isospin surface) of the high-spin ground state of the $[Ni(OH_2)_4]^{2+}$ complex.

$[Ni(OH_2)_6]^{2+}(S),TS$
$E = -627.357\ Hartree$

$[Ni(OH_2)_6]^{2+}(T)$
$E = -627.440\ Hartree$

Figure 11. Optimised geometries of the $[Ni(OH_2)_6]^{2+}$ complexes in their low- and high-spin states computed at the B3LYP level of theory. Bond lengths in Å, bond angles (in italics) in °.
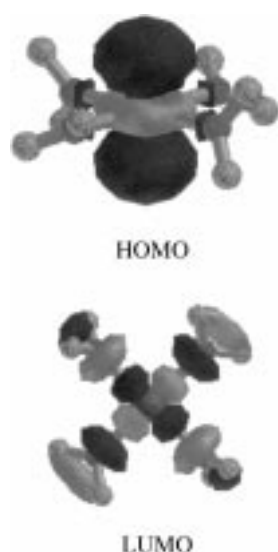
units. The bond overlap populations of the O–H, H···O bonds are 0.16, 0.12 and 0.17, 0.12 for the singly hydrogen-bonded water molecule, and 0.22, 0.06 and 0.23, 0.06 for the doubly hydrogen-bonded water molecule, for the low- and high-spin states respectively The formation of strong hydrogen bonds exhibiting a high covalent component in the singly hydrogen-bonded water molecule is reflected in the computed bond overlap populations, which are almost equivalent for the O–H and H···O bonds. Moreover, as in the case of the tetraaqua Ni^{II} complex in the high-spin state, the Ni^{2+} ion acquires a higher net atomic charge than the singlet state (computed values $+1.19$ and $+0.97$, respectively).

The HOMO at -0.628 eV of the low-spin state corresponds to a central Ni^{2+} atom non-bonding MO with predominantly d_{z^2} character (Figure 14), whereas the LUMO at -0.490 eV corresponds to a hybridised orbital with predominantly $d_{x^2-y^2}$ character directed to the fourth vacant position of the square planar coordination environment of the central Ni^{2+} atom. The form of the LUMO is that expected for a T-shaped three-coordinate fragment resulting from a square planar four-coordinate square planar coordination compound upon removal of one of the ligands. The HOMO–LUMO energy gap is only 0.138 eV.

Surprisingly, as in the case of the tetraaqua Ni^{II} cluster, we have found that the high-spin triplet state of the pentaaqua Ni^{II} cluster, $[Ni(OH_2)_5]^{2+}(T)$ (Figure 10), with a square-pyramidal configuration corresponds to the global minimum in the PES. In the square-pyramidal structure of $[Ni(OH_2)_5]^{2+}(T)$ the central Ni^{2+} atom is found about 0.123 Å above the basal plane defined by four O donor atoms. The square-pyramidal structure of the high-spin ground state is characterised by the dihedral angles O(5)-O(6)-O(4)-O(3) 5.9°, O(5)-O(1)-O(6)-O(3) 84.5°, and O(5)-O(1)-O(6)-O(4) 169.7°. The computed dipole moment is 0.51 D. The Ni–O bond lengths in the high-spin ground state are about 0.2 Å longer than those of the trigonal-planar singlet state. In the triplet state the Ni^{2+} ion and the O donor
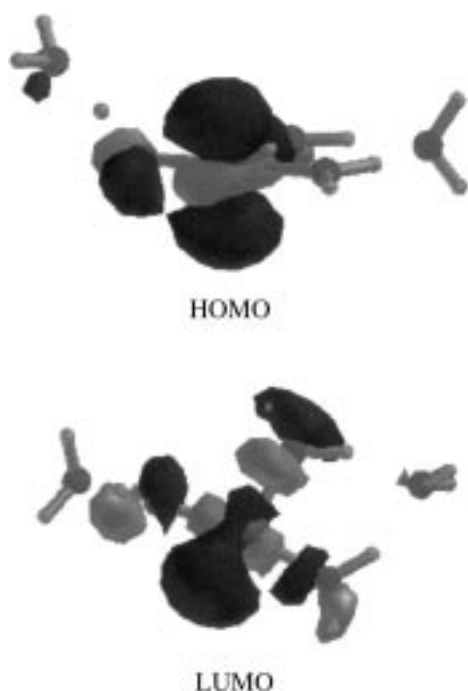

HOMO

LUMO

Figure 12. HOMO and LUMO of the low-spin state of the $[Ni(OH_2)_4]^{2+}$ complex.

HOMO

LUMO

Figure 14. HOMO and LUMO of the low-spin state of the $[Ni(OH_2)_5]^{2+}$ complex.

atoms acquire higher net atomic charges than those in the singlet trigonal-planar state (computed values $+1.05$ and -0.76 respectively). The positive net atomic charge on the H atoms remains unchanged. The bond overlap populations of the Ni−O bonds in the triplet state are 0.02 to 0.05 lower than those in the singlet state, indicating weaker Ni−O bonds (compare also the Ni−O bond lengths). The total atomic spin density is located mainly on the central Ni^{2+} ion (1.79) and much less on the O donor atoms $(0.03 - 0.05)$ (Figure 15).

Figure 15. Atomic spin density (0.002 a.u. isospin surface) of the high-spin ground state of the $[Ni(OH_2)_5]^{2+}$ complex.

However, the computed IFCC values are -30.6 to -38.0 MHz. The two doubly degenerate SOMOs at -0.660 eV correspond to antibonding MOs with predominantly d_{xz} and d_{xy} character, but the LUMO at -0.325 eV corresponds to a central Ni^{2+} atom antibonding MO with predominantly 4s character.

$[Ni(OH_2)_6]^{2+}$ complexes: The low-spin state of the hexaaqua Ni^{II} cluster, $[Ni(OH_2)_6]^{2+}(S)$, exhibiting a square-planar coordination geometry, is a local minimum in the PES,

20.7 kcal mol^{-1} higher in energy than the high-spin triplet ground-state $[Ni(OH_2)_6]^{2+}(T)$ (Figure 11). In the low-spin state of $[Ni(OH_2)_6]^{2+}(S)$, two of the water molecules are not coordinated to the central Ni^{2+} ion but are involved in the formation of short, strong hydrogen bonds with coordinated water molecules, so this species could be formulated as $[Ni(OH_2)_4]^{2+}\cdot 2H_2O$. Importantly, the conformers $[Ni(OH_2)_6]^{2+}(S1)$ and $[Ni(OH_2)_6]^{2+}(S2)$ (Figure 11) have been identified as local minima in the PES of the low-spin state, differing in energy by only 1.9 kcal mol^{-1}.

In the more stable conformer $[Ni(OH_2)_6]^{2+}(S1)$, one water molecule forms a short, strong hydrogen bond with a coordinated water molecule (O−H, H⋯O 1.076, 1.375 Å; bond angle O−H⋯O 2.5°). The second water molecule forms two weaker hydrogen bonds with two coordinated water molecules in *cis* positions: for one, O−H, H⋯O 1.006, 1.669 Å and bond angle O−H⋯O 22.8°, and for the other, O−H, H⋯O 1.005, 1.670 Å and bond angle O−H⋯O 23.8°. The Mulliken net atomic charges on the H atoms involved in hydrogen bond formation are $+0.53$ and $+0.49$ charge units for the O−H⋯O and O−H⋯O⋯H−O skeletons respectively. All other H atoms acquire a net atomic charge of $+0.48$ charge units. The bond overlap populations of the O−H, H⋯O bonds are 0.19, 0.09 for the singly hydrogen-bonded water molecule, and 0.23, 0.05 for the doubly hydrogen-bonded water molecule, respectively. Moreover, the central Ni^{2+} ion acquires a net atomic charge of $+0.86$, whereas the negative net atomic charge on the oxygen atoms is in the -0.73 to -0.79 charge unit range.

In conformer $[Ni(OH_2)_6]^{2+}(S2)$, two water molecules form equivalent short, strong hydrogen bonds with coordinated water molecules in *trans* positions (O−H, H⋯O 1.078, 1.375 Å; bond angle O−H⋯O 1.6°). The $[Ni(OH_2)_6]^{2+}(S2)$ conformer possesses D_{2h} symmetry with the plane defined by the atoms O(5), O(7), O(11) and O(9) being perpendicular to the square planar coordination plane. The computed dipole moment is almost zero (0.02 D). The Mulliken net atomic charges on the H atoms involved in the hydrogen bond formation are $+0.53$, whereas all other H atoms acquire a net atomic charge of $+0.48$ charge units, except those of the water molecules involved in the hydrogen bond formation (net atomic charge 0.46 charge units). The bond overlap populations of the O−H, H⋯O bonds are 0.19, 0.09, respectively. The central Ni^{2+} ion acquires a net atomic charge of $+0.85$, whereas the negative net atomic charge on the oxygen atoms is in the -0.70 to -0.81 charge unit range.

The HOMO at -0.587 eV of the low-spin state corresponds to a central Ni^{2+} atom non-bonding MO with predominantly d_{z^2} character, whereas the LUMO at -0.418 eV corresponds to an antibonding molecular orbital with predominantly $d_{x^2-y^2}$ character. The HOMO−LUMO energy gap is 0.169 eV.

Interestingly, the low-spin state of the hexaaqua Ni^{II} cluster adopting the expected octahedral geometry for a six-coordinate complex of a Ni^{2+} ion was identified as a transition state in the PES (the Hessian matrix has one negative eigenvalue). The transition state, $[Ni(OH_2)_6]^{2+}(S)$, TS, was found to be 31.4 and 52.1 kcal mol^{-1} higher in energy than the more stable low-spin state $[Ni(OH_2)_6]^{2+}(S1)$ and the high-spin ground-state $[Ni(OH_2)_6]^{2+}(T)$, respectively (Figure 11).

The high-spin state of the $[Ni(OH_2)_6]^{2+}$ complex exhibiting an octahedral stereochemistry (D_{2h} point group) is the global minimum in the PES and therefore it is the ground state. The computed dipole moment is almost zero (0.05 D). The six Ni−O bonds, at 2.075 Å, are about 0.2 Å longer than those of the hydrated square-planar singlet states. In the triplet state the Ni^{2+} ion and the O donor atoms acquire higher net atomic charges than those in the singlet state (computed values $+0.93$ and -0.74, respectively). The positive net atomic charge on the H atoms remains unchanged. The bond overlap population of the Ni−O bonds in the triplet state is 0.10. The total atomic spin density is located mainly on the central Ni^{2+} ion (1.79) and much less on the O donor atoms (0.32) (Figure 16). However, the computed IFCC values are -0.0 to -33.2 MHz. The SOMOs at -0.632 eV correspond to the doubly degenerate antibonding MOs with predominantly d_{z^2} and $d_{x^2-y^2}$ character (e_g orbitals in a D_{2h} crystal field), but the LUMO at -0.292 eV corresponds to a central Ni^{2+} atom antibonding MO with predominantly 4s character.

Figure 16. Atomic spin density (0.002 a.u. isospin surface) of the high-spin ground state of the $[Ni(OH_2)_6]^{2+}$ complex.

The incremental binding energy due to the successive addition of one and two water molecules to $[Ni(OH_2)_4]^{2+}$ in the high-spin ground state is 46.4 and 37.6 kcal mol^{-1}, respectively at the B3LYP level. The trends seen for the incremental binding energy are in accordance with those anticipated from electrostatic considerations. The Ni^{II}−water interaction weakens with increasing coordination of the metal. This trend arises from the repulsion of the dipoles between the water ligands and from unfavourable multi-body interactions.

Spectroscopic properties of $[Ni(OH_2)_n]^{2+}$ ($n = 4-6$) complexes: The predicted absorptions (CIS excitation energies) for the high-spin ground states of the $[Ni(OH_2)_n]^{2+}$ ($n = 4-6$) complexes are those expected for the corresponding geometries of the complexes and are in line with experimental data.[52, 53]

For the square-planar $[Ni(OH_2)_4]^{2+}$ (D_{2h}) complex they constitute a band envelope involving crystal field d → d transitions in the 658–945 nm region and ligand-to-metal charge transfer (LMCT) transitions in the 264–283 nm region. In the high-spin square-pyramidal complex $[Ni(OH_2)_5]^{2+}$, the band in the visible region of the spectra (418–542 nm) shows a blue shift relative to the corresponding

band of the $[Ni(OH_2)_4]^{2+}$ complex. In contrast, the MLCT transitions are shifted towards lower frequencies (267–374 nm) relative to the corresponding bands of the four-coordinate square-planar complex. For the octahedral $[Ni(OH_2)_6]^{2+}$ complex the shape of the "middle" band exhibiting two maxima results from the coupling of $E_g(^1E_g)$ and $E_g(^3T_{1g})$ electronic states. As a consequence, the $^3A_{2g} \rightarrow {}^1E_g$ spin-forbidden transition gains significant intensity from the spin-allowed $^3A_{2g} \rightarrow {}^3T_{1g}$ transition, leading to the appearance of a double-humped band envelope.[54] The salient feature of the electronic spectra of the $[Ni(OH_2)_n]^{2+}$ ($n = 4-6$) complexes is the absence of a band around 440–540 nm in the four-coordinate square-planar complexes, whereas this band is shifted towards higher wavelengths in the five-coordinate complex than in the six-coordinate one. Moreover, there is a significant shift of the spin-allowed transitions of $[Ni(OH_2)_5]^{2+}$ at 418.6 and 541.5 nm to higher wavelengths in $[Ni(OH_2)_6]^{2+}$. These features of the electronic spectra of $[Ni(OH_2)_n]^{2+}$ ($n = 4-6$) complexes could be used to distinguish the three different geometries of their high-spin states.

The computed harmonic vibrational frequencies for the high-spin states of $[Ni(OH_2)_n]^{2+}$ ($n = 4-6$) complexes were scaled by 0.96, as suggested previously by Curtiss et al. [55] and Scott and Radom.[56] Their IR spectra of these complexes are characterised by four main bands of vibrational transitions. The first band, in the 3511–3632, 3534–3666 and 3553–3683 cm^{-1} region for the four-, five- and six-coordinated complexes respectively, involves the symmetric, $\nu_{sym}(OH)$, and antisymmetric, $\nu_{asym}(OH)$, stretching vibrations of the O−H bonds. Both stretching vibrations are shifted to higher wavenumbers by increasing the coordination number of the complexes. The second band, in the 1634–1648, 1608–1620 and 1589–1599 cm^{-1} region respectively, involves $\delta(OH)$ stretching vibrations. The third band, in the 572–703, 517–668 and 510–633 cm^{-1} region, respectively, involves skeletal vibrations. The second and third bands are shifted to lower wavenumbers by increasing the coordination number of the complexes. The fourth band, in the 101–451, 115–387 and 111–456 cm^{-1} region, respectively, involves the Ni-O-H out-of-plane vibrations. Thus the position of the IR bands can be used as a criterion for distinguishing the coordination geometry of the $[Ni(OH_2)_n]^{2+}$ ($n = 4-6$) complexes.

Structural, energetic and electronic properties of $[Ni(OH_2)_{n-2}(OH)_2]$ ($n = 4-6$) complexes: Figures 17, 18 and 19 depict the optimised molecular geometries for these complexes in their low- and high-spin states, the latter being the global minima in the PES.

$[Ni(OH_2)_2(OH)_2]$ complexes: The high-spin state of *trans*-$[Ni(OH_2)_2(OH)_2]$, exhibiting a square-planar geometry, is the global minimum in the PES. The low-spin state is a local minimum, at 10.9 kcal mol^{-1} higher in energy than the triplet ground state. Very close to the global minimum (only 1.4 kcal mol^{-1} higher in energy) was found the high-spin state of the *cis* isomer, which surprisingly exhibits a distorted tetrahedral geometry characterised by the dihedral angles O(2)-Ni(1)-O(5)-O(3) 91.2, O(2)-O(4)-Ni(1)-O(3) 89.6 and O(5)-O(3)-Ni(1)-O(4) 149.8°. The low-spin state of the *cis*

Figure 17. Optimised geometries of the *cis*- and *trans*-[Ni(OH$_2$)$_2$(OH)$_2$] isomers in their low- and high-spin states computed at the B3LYP level of theory. Bond lengths in Å, bond angles (in italics) in °.
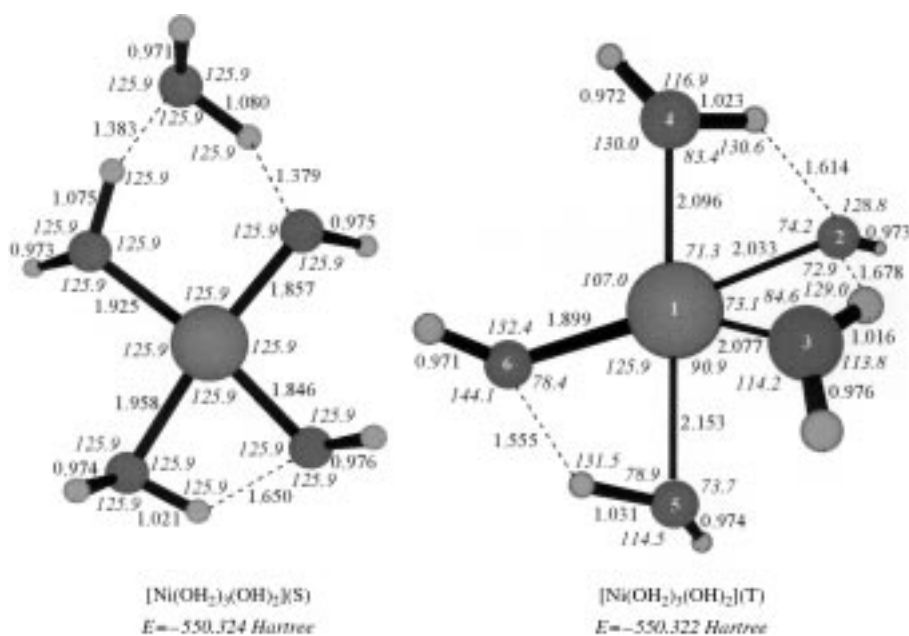
Figure 18. Optimised geometries of the [Ni(OH$_2$)$_3$(OH)$_2$] complexes in their low- and high-spin states computed at the B3LYP level of theory. Bond lengths in Å, bond angles (in italics) in °.

isomer is also a local minimum in the PES, at 10.2 kcal mol^{-1} higher in energy than the ground state, so the low-spin states of the *cis* and *trans* isomers differ by only 0.7 kcal mol^{-1} in energy at the B3LYP level. The most salient feature of the equilibrium geometries of the [Ni(OH$_2$)$_2$(OH)$_2$] isomers is the formation of two intramolecular hydrogen bonds between the coordinated water and hydroxide ligands. In the triplet ground state belonging to the D_{2h} point group, the two O−H bonds are equivalent with O−H and H···O bond lengths of 1.010 and 1.669 Å, respectively. The O−H···O bond angle is 124.0°. The computed zero dipole moment is in accordance with the D_{2h} symmetry. In the high-spin triplet state of the *cis* isomer the two O−H bonds are not equivalent (O−H, H···O 1.008, 1.021 Å and 1.704, 1.612 Å respectively). The O−H···O bond angles are 121.3° and 126.8°, respectively. The computed dipole moment is 2.23 D. The hydrogen bonds of the low-spin states of the two isomers are analogous (Figure 17). The low-spin *cis* and *trans* isomers both adopt square planar geometries with computed dipole moments of 2.23 and 0.00 D respectively. The computed Ni−O bond lengths range from 1.836 to 2.126 Å. The shorter Ni−O bonds correspond to those of the hydroxide ligands (1.836 to 1.874 Å), and the longer ones to the those of the coordinated water ligands (1.928 to 2.126 Å). In all the complexes the hydroxide groups adopt the *anti* configuration.

The Mulliken net atomic charges of the Ni^{2+} ion and the O donor atoms in their triplet states ($q_{Ni} = +0.74$, $q_O = -0.72$, $q_{(O)H} = -0.85$) are higher than those of the singlet states ($q_{Ni} = +0.52$, $q_O = -0.69$, $q_{(O)H} = -0.80$). The positive net atomic charge on the H atoms involved

cis-[Ni(OH₂)₄(OH)₂](S)
E=−626.746 Hartree

cis-[Ni(OH₂)₄(OH)₂](T)
E=−626.773 Hartree

trans-[Ni(OH₂)₄(OH)₂](S)
E=−626.770 Hartree

trans-[Ni(OH₂)₄(OH)₂](T)
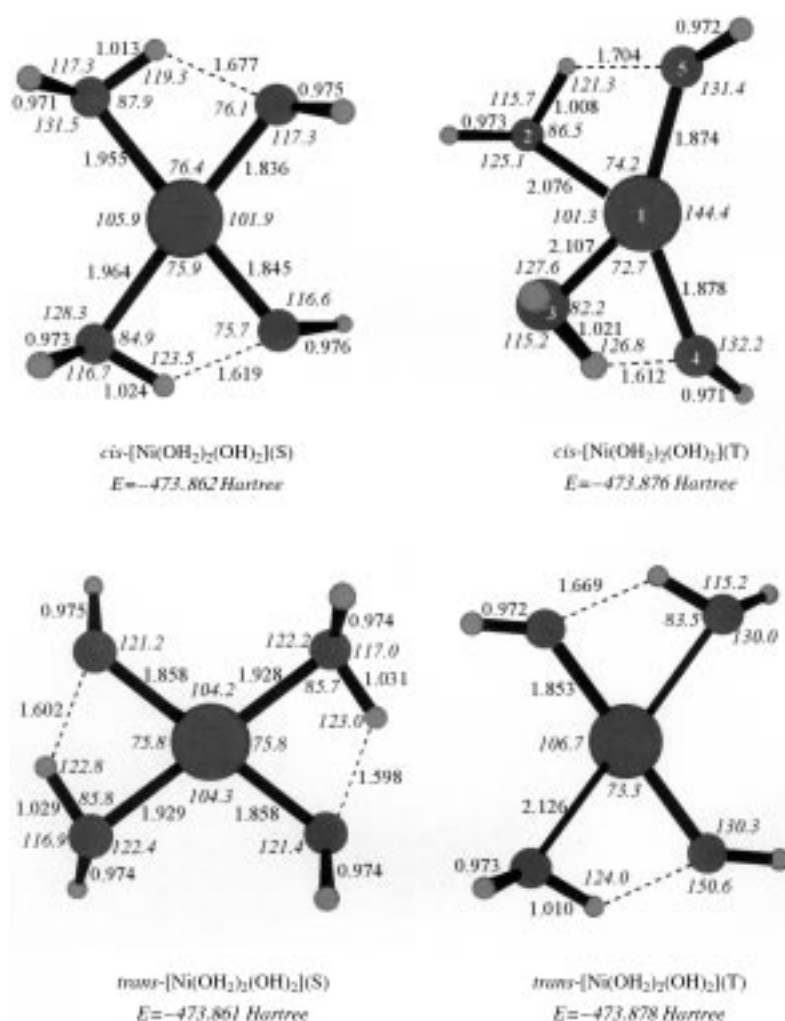E=−626.777 Hartree

Figure 19. Optimised geometries of the *cis*- and *trans*-[Ni(OH₂)₄(OH)₂] isomers in their low- and high-spin states computed at the B3LYP level of theory. Bond lengths in Å, bond angles (in italics) in °.
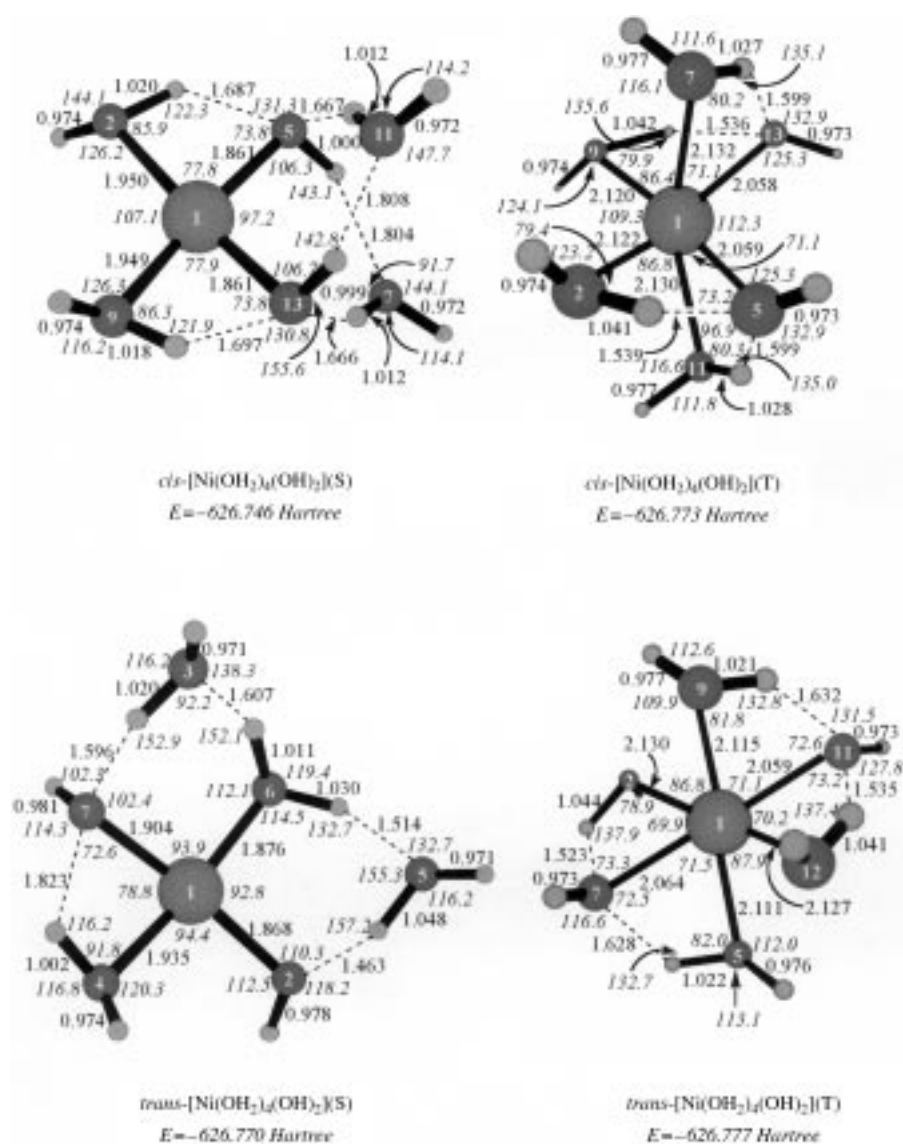

Figure 20. Atomic spin densities (0.002 a.u. isospin surfaces) of the high-spin states of a) *cis*-[Ni(OH₂)₂(OH)₂] and b) *trans*-[Ni(OH₂)₂(OH)₂].

in hydrogen bonds is +0.46. Moreover, the H atoms of the hydroxide groups acquire lower positive net atomic charge (+0.36) than those of the coordinated water ligands (+0.40). The hydroxide ligands clearly have a greater Brønsted-type basicity than the coordinated water ligands. The bond overlap populations of the Ni−OH₂ bonds (0.10) are about half of those for the Ni−OH bonds (0.21). This is a result of the stronger *trans* effect of the hydroxide than the water ligands. The O⋯H bond overlap population is 0.046–0.058. The total atomic spin density is located mainly on the central Ni²⁺ ion (1.61) and much less on the O donor atoms (0.04 for OH₂ and 0.16 for OH) (Figure 20), whereas the computed IFCC values are −0.00, −26.0 and −22.4 MHz for Ni²⁺, OH₂ and OH respectively. The two SOMOs of the triplet ground state at −0.247 and −0.259 eV correspond to antibonding MOs with predominantly metal $d_{x^2-y^2}$ and d_{xz} character, along with a strong component of s AOs located on the O donor atoms of the hydroxide ligands. On the other hand, the LUMO at −0.000 eV corresponds to a non-bonding MO with predom-
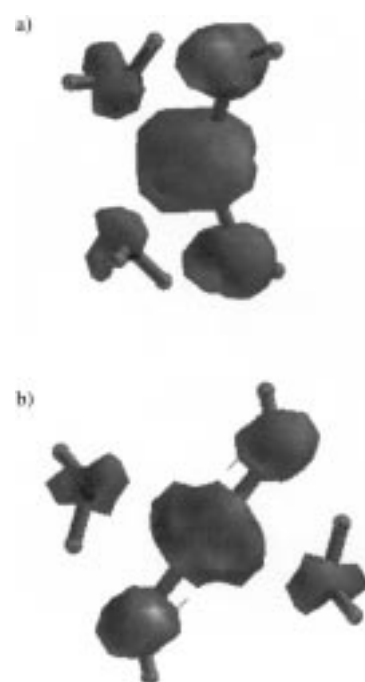
inantly s character localised on one of the H atoms of the coordinated water ligands. Clearly, the H atoms of the coordinated water ligands are more acidic than those of the hydroxide ligands, also being the nucleophilic centre of the complex.

The proton affinity (PA) of the dihydroxy species is calculated from the difference in electronic energies of the protonated $[Ni(OH_2)_n]^{2+}$ and deprotonated $[Ni(OH_2)_{n-2}(OH)_2]$ ($n = 4-6$) complexes [Eq. (1)]. This corresponds to half of the energy of the deprotonation [Eq. (2)], in other words the proton affinity of $[Ni(OH_2)_{n-2}(OH)_2]$ (or, equivalently, the deprotonation energy of $[Ni(OH_2)_n]^{2+}$).

$$PA = \tfrac{1}{2}[E([Ni(OH_2)_{n-2}(OH)_2]) - E([Ni(OH_2)_n]^{2+})] \qquad (1)$$

$$[Ni(OH_2)_n]^{2+} \longrightarrow [Ni(OH_2)_{n-2}(OH)_2] + 2\,H^+ \qquad (2)$$
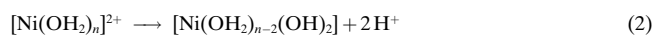
The computed proton affinities of the $[Ni(OH_2)_2(OH)_2]$ complexes of 188.9 and 188.2 kcal mol⁻¹ for the high-spin states, and 184.8 and 185.1 kcal mol⁻¹ for the low-spin states, of the *cis* and *trans* isomers respectively are lower than those of various clusters representing the zeolite ZSM-5, which are relevant to zeolite catalysis because of the catalytic activity of its acid sites.[57–60]

[Ni(OH₂)₃(OH)₂] complexes: The high-spin state of [Ni(OH₂)₃(OH)₂], with a trigonal bipyramidal geometry (Fig-

ure 18), is a local minimum in the PES at 1.3 kcal mol^{-1} higher in energy than the low-spin ground state. In the trigonal-bipyramidal geometry the axial Ni−O bonds are longer than the equatorial ones; the bond angles O(4)-Ni(1)-O(5), O(6)-Ni(1)-O(2) and O(3)-Ni(1)-O(6) are 174.8, 153.8 and 132.5°, respectively. The low-spin state adopts a square-planar stereochemistry with the hydroxide ligands in *cis* positions (a structure similar to that of the low-spin *cis*-[Ni(OH$_2$)$_2$-(OH)$_2$]) but with a water molecule forming two almost equivalent intermolecular hydrogen bonds with one coordinated water molecule and a hydroxide ligand. The hydrogen bonds correspond to O−H, H⋯O bond lengths of 1.075(1.080 Å), 1.383(1.379 Å) and an O−H⋯O bond angle of 125.9°. The Mulliken net atomic charges are +0.46 on the H atoms involved in the hydrogen bond formation, +0.37 on those in the OH group and +0.40 charge units on those of the coordinated water molecules. The HOMO at −0.230 eV of the low-spin state corresponds to a central Ni^{2+} atom non-bonding MO with predominantly d$_{z^2}$ and d$_{xz}$ character, whereas the LUMO at −0.062 eV corresponds to an antibonding orbital with predominantly d$_{x^2-y^2}$ character.

In the triplet state the hydroxide ligands occupy equatorial positions. The salient feature of the structure is that one of the hydroxide ligands forms two intramolecular hydrogen bonds with one equatorial and one axial water ligand. The geometrical parameters of the hydrogen bonds are shown in Figure 18. The Mulliken net atomic charges are +0.46 on the H atoms involved in the hydrogen bond formation, +0.36 on those in the OH groups and 0.38−0.40 charge units on those of the coordinated water molecules. The total atomic spin density is located mainly (1.67) on the central Ni^{2+} ion and much less (0.04−0.13) on the O donor atoms (Figure 21). The computed IFCC values are −0.00, −18.8−25.7 and

Figure 21. Atomic spin density (0.002 a.u. isospin surface) of the high-spin ground state of the [Ni(OH$_2$)$_3$(OH)$_2$] complex.

−20.2 MHz for Ni^{2+}, OH$_2$ and OH respectively. The two SOMOs at −0.249 and −0.259 eV correspond to central Ni^{2+} atom antibonding MOs with predominantly d$_{x^2-y^2}$, d$_{xz}$, d$_{yz}$ and d$_{xy}$, d$_{x^2-y^2}$, d$_{xz}$ character respectively. The high degree of mixing of the AOs is due to the low symmetry of the complex. The LUMO at −0.002 eV corresponds to a non-bonding orbital with predominantly s character localised on the H atom of one of the hydroxide ligands.

The computed PAs of [Ni(OH$_2$)$_3$(OH)$_2$] are 182.0 and 202.0 kcal mol^{-1} for the low- and high-spin states, respectively, very close to those of the [Ni(OH$_2$)$_2$(OH)$_2$] complexes.

[Ni(OH$_2$)$_4$(OH)$_2$] complexes: The *cis* and *trans* isomers of [Ni(OH$_2$)$_4$(OH)$_2$] have been investigated in both their high- and low-spin states. The high-spin triplet state of *trans*-[Ni(OH$_2$)$_4$(OH)$_2$] corresponds to a global minimum in the PES, whereas the singlet state of the *trans* isomer is a local minimum 4.4 kcal mol^{-1} higher in energy than the triplet ground state. The triplet state of *cis*-[Ni(OH$_2$)$_4$(OH)$_2$] was found to be only 2.5 kcal mol^{-1} above the triplet ground state of *trans*-[Ni(OH$_2$)$_4$(OH)$_2$]. The singlet state of *cis*-[Ni(OH$_2$)$_4$-(OH)$_2$] is also a local minimum, being 19.5 kcal mol^{-1} higher in energy than the triplet ground state. The high-spin states of both isomers adopt distorted octahedral geometries, whereas the low-spin states exhibit essentially square-planar geometries with two water molecules not involved in the coordination sphere. These water molecules are involved only in intermolecular hydrogen bonding with the hydroxide and/or the coordinated water ligands. Therefore, the low-spin states of [Ni(OH$_2$)$_4$(OH)$_2$] correspond to the formula Ni(OH$_2$)$_2$-(OH)$_2$·2H$_2$O.

In all the structures, both hydroxide ligands are involved in the formation of hydrogen bonds with adjacent coordinated water ligands. It is important that the hydroxide ligands form two intra- and/or intermolecular hydrogen bonds with adjacent water ligands simultaneously, the only exception being the low-spin *trans* isomer in which one of the hydroxide ligands is involved in one intermolecular hydrogen bond. The characteristics of the hydrogen bonds are shown in Figure 19. In the low-spin state of the *cis* isomer the non-coordinated water molecules forming the intermolecular hydrogen bonds are located above and below the coordination plane, with dihedral angles O(5)-Ni(1)-O(13)-O(11) 44.3° and O(5)-Ni(1)-O(13)-O(7) −45.7°. In contrast, in the low-spin state of the *trans* isomer both non-coordinated water molecules are located above the coordination plane, with dihedral angles O(5)-O(2)-Ni(1)-O(6) 3.4° and O(3)-O(6)-Ni(1)-O(7) 27.5°.

The HOMO of the low-spin states of the *cis* and *trans* isomers at −0.239 and −0.243 eV, respectively, correspond to central Ni^{2+} atom antibonding MOs with predominantly d$_{z^2}$ character. However, the LUMOs at −0.069 and −0.068 eV correspond to antibonding MOs with predominantly d$_{x^2-y^2}$ character. The SOMOs of the high-spin states of the *cis* (*trans*) isomers at −0.247(−0.247) eV correspond to antibonding MOs resulting from the mixing of d$_{xz}$ and d$_{yz}$ AOs of the central Ni^{2+} ion and p$_x$ AOs localised on the O donor atoms of the hydroxide ligands. The SOMOs at −0.264(−0.267) correspond to antibonding MOs resulting from the mixing of d$_{x^2-y^2}$ and d$_{xy}$ AOs of the Ni^{2+} ion and p$_x$ AOs localised on the O donor atoms of the hydroxide ligands. The LUMO at 0.009(0.008) eV is a non-bonding MO localised on the H atoms of the equatorial O donor atoms of the water ligands. The total atomic spin densities of the high-spin states of the *cis* and *trans* isomers are located mainly on the central Ni^{2+} ion (1.675 for both isomers) and much less on the O donor atoms (0.04−0.08), being higher for the O donor atoms of the hydroxide ligands (Figure 22). The computed IFCC values of the *cis*(*trans*) isomers are −0.00(−0.00), −17.4(−18.4) and −21.0(−20.0) MHz for Ni^{2+}, OH$_2$ and OH, respectively.
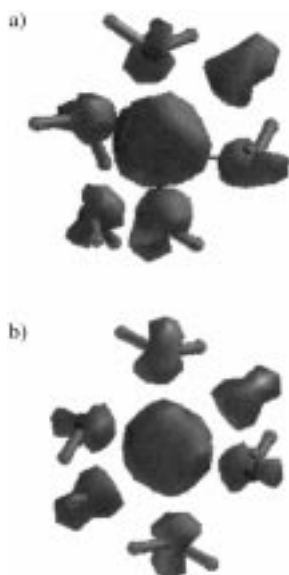
Figure 22. Atomic spin densities (0.002 a.u. isospin surfaces) of the high-spin states of a) cis-[Ni(OH$_2$)$_4$(OH)$_2$] and b) $trans$-[Ni(OH$_2$)$_4$(OH)$_2$].

The incremental binding energies due to the successive addition of water molecules to [Ni(OH$_2$)$_2$(OH)$_2$] in the triplet ground states are 18.8 and 22.8 kcal mol^{-1} for the first and second, respectively, being much lower than those of the [Ni(OH$_2$)$_n$]$^{2+}$ compounds. Moreover, the trends in the incremental binding energy follow inversely the order of the [Ni(OH$_2$)$_n$]$^{2+}$ compounds. This is not unexpected, as the successive addition of water ligands to [Ni(OH$_2$)$_2$(OH)$_2$] increases the number of hydrogen bonds formed, thus stabilizing the complexes with increasing coordination number. The computed PAs of [Ni(OH$_2$)$_4$(OH)$_2$] are 209.3 and 208.0 kcal mol^{-1} for the high-spin states of the cis and $trans$ isomers respectively. The PA generally increases with increasing coordination number of the complexes.

Spectroscopic properties of [Ni(OH$_2$)$_{n-2}$(OH)$_2$] ($n = 4 - 6$) complexes: The predicted absorptions (CIS excitation energies) for the high-spin ground states of these complexes are those expected for the corresponding geometries of the complexes and are in line with experimental data.[52]

There are remarkable differences between the spectra of the dihydroxy derivatives and those of the corresponding unprotonated aqua complexes. The electronic spectrum of the four-coordinate [Ni(OH$_2$)$_{n-2}$(OH)$_2$] complex exhibits two extra absorption bands with maxima at 966 and 337 nm, which do not exist in the spectrum of the [Ni(OH$_2$)$_4$]$^{2+}$ complex. In the spectrum of the five-coordinate [Ni(OH$_2$)$_3$(OH)$_2$] complex there are two absorption bands with maxima at 762.2 and 602.3 nm, which do not exist in the spectrum of the [Ni(OH$_2$)$_5$]$^{2+}$ complex. The spectrum of the six-coordinate [Ni(OH$_2$)$_4$(OH)$_2$] is similar to that of the corresponding hexaaqua complex. The electronic spectra of [Ni(OH$_2$)$_n$]$^{2+}$ and [Ni(OH$_2$)$_{n-2}$(OH)$_2$] ($n = 4 - 6$) complexes could therefore be used to distinguish their various geometries.

From comparison of the calculated spectra with the experimentally determined UV/Vis absorption spectrum of the NiHEU zeolitic material involving three absorption bands at 755.9 nm (shoulder), 667.3 nm and 385.7 nm, it can be concluded that the nickel-containing species incorporated into the zeolite structure corresponds to the [Ni(OH$_2$)$_2$(OH)$_2$] complex (either cis or $trans$ isomers), probably chemisorbed on the surface through a fifth coordination to a bridging O atom of the zeolite framework, in line with all the other experimental data discussed so far.

The computed IR spectra of [Ni(OH$_2$)$_{n-2}$(OH)$_2$] ($n = 4 - 6$) complexes exhibit the main features of the spectra of the corresponding [Ni(OH$_2$)$_n$]$^{2+}$ ($n = 4 - 6$) complexes, but involve some extra bands attributable to the hydroxide ligands. Thus, the band in the 2968 – 3084, 2707 – 2967 and 2520 – 2872 cm^{-1} region for the four-, five- and six-coordinate complexes respectively involves the stretching, ν(OH), vibrations of the O$\cdots$H bonds, which are shifted to lower wavenumbers by increasing the coordination number of the complexes. The band in the 1474 – 1486, 1473 – 1500 and 1510 – 1570 cm^{-1} region for the four-, five- and six-coordinate complexes, respectively, involves δ(OH) stretching vibrations, which are shifted to higher wavenumbers by increasing the coordination number of the complexes. The band in the 882 – 984, 859 – 965 and 722 – 996 cm^{-1} region for the four-, five- and six-coordinate complexes, respectively, is attributed to skeletal and out-of-plane vibrations. Thus the position of the IR bands can be used as a criterion for distinguishing the coordination geometry of the [Ni(OH$_2$)$_n$]$^{2+}$ ($n = 4 - 6$) complexes.

Conclusion

In this work a carefully selected combination of experimental (XRF, SEM-EDS, FT-IR, DR(UV/Vis)S and XPS measurements) and theoretical (DFT) tools has been used to characterize nickel-loaded HEU-type zeolite crystals as non-homoionic and non-stoichiometric, containing exchangeable hydrated Ni^{2+} ions in the micropores and nickel hydroxide phases supported on the surface. Moreover, TGA/DTG and DTA techniques have demonstrated that full dehydration occurs below approximately 400 °C following a clear endothermic process, whereas at higher temperatures the zeolite is amorphised and finally partially recrystallised to Ni(Al,Si) oxides (detected by powder XRD). The solid acidity of NiHEU, determined experimentally, is due to the existence of both weak acid sites (fundamentally Lewis sites) resolved at approximately 183 °C, and strong acid sites (essentially Brønsted sites) resolved at approximately 461 °C, in the TPD pattern. A more sophisticated study, by in situ/ex situ FT-IR in combination with in situ/ex situ ^{27}Al MAS NMR with Py as a probe molecule, revealed that the Lewis acid sites could be attributed primarily to Ni^{2+} ions, whereas the Brønsted ones could not be associated with possible bridging hydroxyls but probably with the surface-supported nickel hydroxide phases. The spectroscopic measurements in conjunction with powder XRD and ^{29}Si MAS NMR data strongly suggest that distorted Al tetrahedra are formed during the dehydration process and Py chemisorption/complexation (NiHEU-Py), whereas the crystal structure is remarkably preserved in the rehydrated material (NiHEU-Py/R). The structural, electronic, energetic

and spectroscopic properties of all possible aqua and dihydroxy nickel(II) complexes absorbed in the zeolite micropores or supported on the zeolite surface were studied theoretically by DFT calculations and discussed in relation to experimental data. According to theoretical results the most likely species to be chemisorbed on the zeolite's surface is the $[Ni(OH_2)_2(OH)_2]$ complex, thus substantiating the experimental spectroscopic properties (FT-IR and UV/Vis absorption spectra) of the NiHEU zeolite. The computed proton affinities found in the $182.0 - 210.0$ kcal mol^{-1} range increase with increasing coordination number of the dihydroxy aqua complexes.

Acknowledgement

[1] R. Szostak, *Handbook of Molecular Sieves*, Van Nostrand Reinhold, New York, **1992**.

[2] W. M. Meier, D. H. Olson, C. Baerlocher, *Atlas of Zeolite Structure Types*, 4th Ed., Elsevier, London, **1996**.

[3] *Mineralogy and Geology of Natural Zeolites*, Vol. 4 of *M.S.A. Short Course Notes*, Ed.: F. A. Mumpton, M.S.A., Washington D.C., **1977**.

[4] G. Gottardi, E. Galli, *Natural Zeolites*, Springer-Verlag, Berlin, **1985**.

[5] R. Tschernich, *Zeolites of the World*, Geoscience Press, Phoenix, AR, **1992**.

[6] G. V. Tsitsishvili, T. G. Andronikashvili, G. N. Kirov, L. D. Filizova, *Natural Zeolites*, Ellis Horwood, Chichester, **1992**.

[7] D. W. Breck, *Zeolite Molecular Sieves: Structure, Chemistry and Use*, Wiley, New York, **1974**.

[8] R. M. Barrer, *Zeolites and Clay Minerals as Sorbents and Molecular Sieves*, Academic Press, London, **1978**.

[9] J. Griffiths, *Ind. Miner.* **1987**, *87*, 19.

[10] A. Dyer, *Zeolite Molecular Sieves*, Wiley, Chichester, **1988**.

[11] *Natural Zeolite and its Utilisation*, (Ed.: H. Minato), Tokyo, **1994**.

[12] *Natural Microporous Materials in Environmental Technology* (Eds.: P. Misaelides, F. Macásek, T. Pinnavaia, C. Colella), Kluwer, Dordrecht, **1999**.

[13] D. W. Breck, G. W. Skeels, US Patent 4503023, **1985**.

[14] S. Khodabandeh, S. Davis, *Micropor. Mater.* **1997**, *9*, 149.

[15] C. D. Williams, *Chem. Commun.* **1997**, 2113.

[16] D. Y. Zhao, K. Cleare, C. Oliver, C. Ingram, D. Cook, R. Szostak, L. Kevan, *Micropor. Mesopor. Mater.* **1998**, *21*, 371.

[17] a) U. Ventriglia, *Period. Mineral. Roma* **1955**, *24*, 49; b) A. B. Merkle, M. Slaughter, *Am. Mineral.* **1968**, *53*, 1120; c) A. Alberti, *Tschermaks Min. Petr. Mitt.* **1972**, *18*, 129; d) A. Alberti, *Tschermaks Min. Petr. Mitt.* **1972**, *22*, 25; e) H. Bartl, *Z. Kristallogr.* **1973**, *137*, 440; f) K. Koyama, Y. Takeuchi, *Z. Kristallogr.* **1977**, *145*, 216; g) O. Petrov, T. Karamaneva, G. Kirov, *C. R. Acad. Bulgare Sci.* **1984**, *37*, 785; h) T. W. Hambley, J. C. Taylor, *J. Solid State Chem.* **1984**, *54*, 1; i) T. Armbruster, M. E. Gunter, *Am. Mineral.* **1991**, *76*, 1872; j) T. Armbruster, *Am. Mineral.* **1993**, *78*, 260; k) M. Slaughter, J.-Y. Yu, in *Natural Zeolites '93*, Eds.: D. W. Ming, F. A. Mumpton, Int. Committ. Nat. Zeolites, New York, **1995**, p. 209.

[18] J. V. Smith, *Chem. Rev.* **1988**, *88*, 149.

[19] J. V. Smith in *Zeolites: Facts, Figures, Future* (Eds.: P. A. Jacobs, R. A. van Santen), Elsevier, Amsterdam, **1989**, p. 29.

[20] H. van Koningsveld in *Introduction to Zeolite Science and Practice* (Eds.: H. van Bekkum, P. A. Jacobs, E. M. Flanigen, J. C. Jansen), Elsevier, Amsterdam, **1991**, p. 35.

[21] R. M. Barrer in *Natural Zeolites: Occurrence, Properties, Use* (Eds.: L. B. Sand, F. A. Mumpton), Pergamon, Oxford, **1978**, p. 385.

[22] a) Z. V. Gryaznova, G. V. Tsitsishvili, S. I. S. Sidamonidze, L. G. Akhalbedashvili, Z. I. Koridze, in *Natural Zeolites* (Ed.: F. I. Brouchek), Tbilisi, Georgia (USSR), **1979**, p. 207; b) R. Roque-Malherbe, C. de las Pozas, G. Rodriguez, G. M. Plavnik, *Rev. Cubana Fis.* **1984**, *4*, 135; c) D. Kalló in *Occurrence, Properties and Utilisation of Natural Zeolites* (Eds.: D. Kalló, H. S. Sherry), Akadémiai Kiadó, Budapest, **1988**, p. 601; d) Y. Goto, T. Matsumoto, F. Iso, *Nendo Kagaku* **1994**, *32*, 102; e) G. O. Chivadze, G. V. Tsitsishvili, V. G. Metreveli, T. I. Naskidashvili in *Book of Extended Abstracts of Sofia Zeolite Meeting '95* (Ed.: G. N. Kirov), Sofia, **1995**, p. 65; f) M. Travieso, G. Liabré, J. A. Gonzàlez, A. Arcoya, X. L. Seoane in *Zeolites '91* (Eds.: G. R. Fuentes, J. A. Gonzàles), Havana, **1991**, p. 150; g) A. Arcoya, J. A. Gonzàlez, G. Liabré, X. L. Seoane, M. Travieso in *Zeolites '91* (Eds.: G. R. Fuentes, J. A. Gonzàles), Havana, **1991**, p. 289; h) C. de las Pozas, R. Lopez-Cordero, C. Diaz-Aguila, M. Cora, R. Roque-Malherbe, *J. Solid State Chem.* **1995**, *114*, 108; i) A. Arcoya, X. L. Seoane, J. Soria, *J. Chem. Tech. Biotechnol.* **1997**, *68*, 171.

[23] a) N. Bresciani-Pahor, M. Calligaris, G. Nardin, L. Randaccio, E Russo, P. Comin-Chiaramonti, *J. Chem. Soc. Dalton Trans.* **1980**, 1511; b) N. Bresciani-Pahor, M. Calligaris, G. Nardin, L. Randaccio, *J. Chem. Soc. Dalton Trans.* **1981**, 309; c) E. Galli, G. Gottardi, H. Mayer, A. Preisinger, E. Passaglia, *Acta Crystallogr. Sect. B* **1983**, *39*, 189; d) O. Petrov, L. Filizova, G. Kirov, *C. R. Acad. Bulgare Sci.* **1985**, *38*, 603; e) K. Sugiyama, Y. Takeuchi in *New Developments in Zeolite Science and Technology* (Eds.: Y. Murakami, A. Iijima, J. W. Ward), Kodansha, Tokyo/Elsevier, Amsterdam, **1986**, p. 449; f) J. R. Smyth, A. T. Spaid, D. L. Bish, *Am. Mineral.* **1990**, *75*, 522; g) O. Petrov, L. Filizova, G. Kirov, *C. R. Acad. Bulgare Sci.* **1991**, *44*, 77; h) M. E. Gunter, T. Armbruster, T. Kohler, C. R. Knowles, *Am. Mineral.* **1994**, *79*, 675; i) O. Petrov in *Natural Zeolites '93* (Eds.: D. W. Ming, F. A. Mumpton), *Int. Committ. Nat. Zeolites*, New York, **1995**, p. 271; j) P. Yang, T. Armbruster, *J. Solid State Chem.* **1996**, *123*, 140; k) J. Stolz, T. Armbruster in *Book of Abstracts of Zeolite '97* (Eds: C. Colella), Naples, **1997**, p. 273; l) J. Stolz, P. Yangand, T. Armbruster, *Micropor. Mesopor. Mater.* **2000**, *37*, 233.

[24] A. Godelitsas, J. Dwyer, D. Charistos, A. Filippidis, C. Tsipis in *Book of Abstracts of NATO – ASI on New Trends in Materials Chemistry* (Ed.: R. Catlow), NATO – ASI, Il Ciocco, **1995**, p. 49.

[25] a) A. D. Becke, *Phys. Rev. A* **1988**, *38*, 3098; b) C. Lee, W. Yang, R. G. Parr, *Phys. Rev. B* **1988**, *37*, 785; c) S. H. Vosko, L. Wilk, M. Nussair, *Can. J. Phys.* **1980**, *58*, 1200; d) A. D. Becke, *J. Chem. Phys.* **1993**, *98*, 5648.

[26] a) J. B. Nicholas, *Top. Catal.* **1997**, *4*, 157; b) W. Koch, R. H. Hertwing, *Chem. Phys. Lett.* **1997**, *286*, 345; c) L. A. Curtis, K. Raghavachari, P. C. Redfern, J. A. Pople, *Chem. Phys. Lett.* **1997**, *270*, 419; d) D. M. Smith, B. T. Golding, L. Radom, *J. Am. Chem. Soc.* **1999**, *121*, 9388; e) A. K. Chandra, M. T. Nguyen, *Chem. Phys.* **1998**, *232*, 299; f) J. B. Nicholas, *Top. Catal.* **1999**, *9*, 181; g) R. Arnaud, C. Adamo, M. Cossi, A. Millet, Y. Vallé, V. Barone, *J. Am. Chem. Soc.* **2000**, *122*, 324.

[27] H. B. Schlegel, *J. Comput. Chem.* **1982**, *3*, 214.

[28] M. J. Frisch, G. W. Trucks, H. B. Schlegel, G. E. Scusseria, M. A. Robb, J. R. Cheeseman, V. G. Zakrzewski, J. A. Montgomery, R. E. Stratmann, J. C. Burant, S. Dapprich, J. M. Millan, A. D. Daniels, K. N. Kudin, M. C. Strain, O. Farkas, J. Tomasi, V. Barone, M. Cossi, R. Cammi, B. Mennucci, C. Pomelli, C. Adamo, S. Clifford, J. Orchterski, G. A. Petersson, P. Y. Ayala, Q. Cui, K. Morokuma, D. K. Malick, A. D. Rabuck, K. Raghavachari, J. B. Foresman, J. Cioslowski, J. V. Ortiz, B. B. Stefanov, G. Liu, A. Liashenko, P. Piskorz, I. Komaroni, R. Gomperts, R. L. Martin, D. J. Fox, T. Keith, M. A. Al-Laham, C. Y. Peng, A. Nanayakkara, C. Gonzalez, M. Challacombe, P. M. Gill, P. Johnson, W. Chen, M. W. Wong, J. L. Andres, M. Head-Gordon, E. S. Replogle, J. A. Pople, Gaussian 98, Revision A.4, Gaussian Inc., Pittsburgh, PA, **1998**.

[29] *Handbook of X-Ray Photoelectron Spectroscopy* (Eds.: C. D. Wagner, W. M. Riggs, L. E. Davis, M. F. Moulder, G. E. Muilenberg), Perkin-Elmer, New York, **1979**.

[30] *Practical Surface Analysis* (Eds.: D. Briggs, M. P. Seah), Wiley, New York, **1983**.

[31] *Methods of Surface Analysis* (Ed.: J. M. Walls), Cambridge University Press, Cambridge, **1990**.

[32] M. Stöcker, *Micropor. Mater.* **1996**, *6*, 235.

[33] Y. I. Ryskin in *The Infrared Spectra of Minerals*, (Ed.: V. C. Farmer), Monograph 4, Mineralogical Society, London, **1974**, p. 137.

[34] M. M. J. Treacy, J. B. Higgins, R. von Ballmoos, *Collection of Simulated XRD Powder Patterns for Zeolites*, 3rd ed., Int. Zeolite Assoc., Elsevier, London, **1996**.

[35] W. Stumm, *Chemisty of the Solid – Water Interface: Processes at the Mineral – Water and Particle – Water Interface in Natural Systems*, John Wiley, New York, **1992**.

[36] G. E. Brown Jr., G. A. Parks, P. A. O'Day, in *Mineral Surfaces*, (Eds.: D. J. Vaughan, R. A. D. Pattrick), Chapman and Hall, London, **1995**, p. 129.

[37] C. F. Baes Jr., R. E. Mesmer, *Hydrolysis of Cations*, R. E. Krieger, Malabar, **1986**.

[38] R. A. Schoonheydt, L. J. Vandamme, P. A. Jacobs, J. B. Uytterhoeven, *J. Catal.* **1976**, *43*, 292.

[39] S. Xiao and Z. Meng, *J. Chem. Soc. Faraday Trans.* **1994**, *90*, 2591.

[40] E. R. Nightingale, *J. Phys. Chem.* **1959**, *63*, 138.

[41] E. D. Garbowski, C. Mirodatos, M. Primet, M. V. Mathleu, *J. Phys. Chem.* **1983**, *87*, 303.

[42] G. Engelhardt, D. Michel, *High-Resolution Solid State NMR of Silicates and Zeolites*, Wiley, Chichester, **1987**.

[43] E. Lippmaa, M. Mägi, A. Samoson, M. Tarmak, G. Engelhardt, *J. Am. Chem. Soc.* **1981**, *103*, 4992 .

[44] R. L. Ward , H. L. McKague, *J. Phys. Chem.* **1994**, *98*, 1232.

[45] J. W. Ward, in *Zeolite Chemistry and Catalysis* (Ed.: J. Rabo), Monograph No. 171, American Chemical Society, Washington D.C., **1976**, , p. 118.

[46] J. Dwyer, in *Innovation in Zeolite Materials Science* (Eds.: P. J. Grobet, W. J. Mortier), Elsevier, Amsterdam, **1988**, p. 333.

[47] H. G. Karge in *Catalysis and Adsorption by Zeolites* (Eds.: G. Öhlmann, H. Pfeifer, R. Fricke), Elsevier, Amsterdam, **1991**, p. 133.

[48] W. E. Farneth, R. J. Gorte, *Chem. Rev.* **1995**, *95*, 615.

[49] J. Connerton, R. W. Joyner, M. B. Padley, *J. Chem. Soc. Faraday Trans.* **1995**, *91*, 1841.

[50] B. Zibrowius, U. Lohse, J. Richter-Mendau, *J. Chem. Soc. Faraday Trans.* **1991**, *87*, 1433.

[51] L. Rulíšek, Z. Havlas, *J. Am. Chem. Soc.* **2000**, *122*, 10428.

[52] a) A. B. P. Lever, *Inorganic Electronic Spectroscopy*, Elsevier, Amsterdam, **1984**, p. 507; b) C. K. Jorgensen, *Absorption Spectra and Chemical Bonding in Complexes*, Pergamon, Oxford, **1964**, p. 297.

[53] B. Coughlan, W. A. McCann, W. M. Carroll, *J. Colloid Interface Sci.* **1977**, *87*, 1433.

[54] a) M. Triest, G. Bussière, H. Bélisle, C. Reber, *J. Chem. Educ.* **2000**, *77*, 670; b) G. Bussière, C. Reber, *J. Am. Chem. Soc.* **1998**, *120*, 6306; c) R. Stranger, K. L. McMahon, L. R. Graham, J. I. Bruce, T. W. Hambley, *Inorg. Chem.* **1997**, *36*, 3466; d) W. P. Anderson W. D. Edwards, M. C. Zerner, *Inorg. Chem.* **1986**, *25*, 2728.

[55] L. A. Curtiss, K. Raghavachari, P. C. Redfern, J. A. Pople, *Chem. Phys. Lett.* **1997**, *270*, 419.

[56] A. P. Scott, L. Random, *J. Chem. Phys.* **1996**, *100*, 16502.

[57] N. O. Gonzales, A. T. Bell, A. K. Chakraborty, *J. Phys. Chem.* **1997**, *101*, 10058.

[58] H. V. Brand, L. A. Curtiss, L. E. Iton, *J. Phys. Chem.* **1993**, *97*, 12773.

[59] G. J. Kramer, R. A. van Santen, *J. Am. Chem. Soc.* **1993**, *115*, 2887.

[60] M. Brandle, J. Sauer, *J. Am. Chem. Soc.* **1998**, *120*, 1556.